WEAR AND CORROSION BEHAVIOR OF SPARK PLASMA SINTERED IRON-BASED BULK METALLIC GLASS COMPOSITES AND COATINGS

By

HIMABINDU KASTURI

Bachelor of Science in Mechanical Engineering

Osmania University

Hyderabad, INDIA

2014

Submitted to the Faculty of the
Graduate College of the
Oklahoma State University
in partial fulfillment of
the requirements for
the Degree of
MASTER OF SCIENCE
July 2018

WEAR AND CORROSION BEHAVIOUR OF SPARK PLASMA SINTERED IRON-BASED BULK METALLIC GLASS COMPOSITES AND COATINGS

Thesis Approved:

Dr. Sandip P. Harimkar

Thesis Adviser

Dr. Hitesh D. Vora

Dr. Shuodao Wang

Acknowledgments

I would like to express my gratitude and thank my advisor Dr. Sandip Harimkar, for giving the opportunity to work on novel materials such as metallic glasses. For allowing me to explore various fields of material science and for his continuous, patient support throughout my master's program, I consider myself fortunate to have worked under him. He is an inspiration for his meticulous approach towards projects. He encourages and offers his unwavering support to his students, to pursue new and challenging fields of study.

For presenting me with this opportunity, I am immensely thankful to Oklahoma State University and the U.S. National Science Foundation. This material is based upon work supported by the National Science Foundation under Grant No. CMMI -1462602. This tremendous initiative has encouraged students like me from across different nations to work and learn in challenging environments. This opened doors to promising avenues, giving an opportunity to grow in our careers and as individuals.

This thesis would not have been complete without the guidance of Tanaji Paul. His mentorship has been invaluable. His practical approach towards projects, detailed planning, and comprehensive technical knowledge will always inspire me. For his never-ending support, for being extremely patient in all our discussions, for teaching me to be methodical and detail oriented and being a friend and a colleague, I express my most sincere Thank you and gratitude.

To Sourabh Biswas, for being a wonderful and extremely supportive colleague and a great teacher, I thank you for all your advice. It was your continuous guidance that helped me find answers to a lot of my questions during my time as a Teaching assistant. For all your valuable advice and support regarding my research and career, and for everything I have learned, you have my heartfelt thanks.

I thank S. Habib Alavi for inspiring me to work harder. His knowledge and dedication towards research are awe-inspiring and a constant motivation.

I thank the almighty for providing me a home away from home. To all my friends, the past two years were memorable because of your company. You provided me with a constant support system and a ton of memories to carry forward. I am grateful for your

company and all that you've taught me.

I will fall short of words to express my gratitude to my family. I do not believe saying a simple thank you is enough. I owe you for making me the person I am today. You are my backbone and my motivation to become a better person every single day. I will always strive to make you proud and keep you happy.

Name: HIMABINDU KASTURI

Date of Degree: JULY 2018

Title of Study: WEAR AND CORROSION BEHAVIOR OF SPARK PLASMA SINTERED IRON-BASED BULK METALLIC GLASS COMPOSITES AND COATINGS

Major Field: Mechanical and Aerospace Engineering

Abstract: Bulk metallic glasses (BMGs) exhibit exceptional strength, hardness and wear and corrosion resistance due to their disordered atomic structure. Various Zr-, Ni-, Ti-, Cu- and Fe- based BMGs were processed using rapid solidification techniques. However, high cooling rates necessary in conventional solidification methods limit the critical diameter of the alloy to a few centimeters. Spark plasma sintering (SPS) provides an alternate solid-state processing approach without the need for high cooling rates because of mechanisms such as Joule heating, making use of pulsed direct current. This enables processing of fully dense BMG's. This technique has been extensively employed to process Cu-, Ti- and Zr-based metallic glasses, their composites, and coatings. In order to utilize the availability of inexpensive Fe-based metallic glasses with excellent mechanical properties, this thesis investigates the processing and evaluation of wear and corrosion resistant composites and coatings of $Fe_{48}Cr_{15}Mo_{14}Y_2C_{15}B_6$ metallic glass. Spark plasma sintered metallic glass composites exhibited anodic polarization in corrosive chloride environment and highest wear resistance with 5 vol.% Ni reinforcement. Coatings of this metallic glass on Cu-Ni alloy exhibited the lowest wear upon processing just below the crystallization temperature. Therefore, this study validates SPS as a promising solid-state processing route to manufacture Fe-based metallic glass composites and coatings.

TABLE OF CONTENTS

LIST OF TABLES

LIST OF FIGURES

CHAPTER I

BULK METALLIC GLASSES- PROCESSING AND PROPERTIES

1.1 Introduction

Metals occupy a prominent role in the development of human civilization, where they can be found in every nook and corner of our day-to-day life. The practice of metal extraction and forging it in various shapes for application was established a few thousands of years ago. The Copper, Bronze, and Iron Ages established primitive methods of metal extraction and processing, to meet the day-to-day requirements. One of the most common modes of material extraction and manufacturing, i.e. smelting and casting were widely employed during these eras. It was also during this period, that the possibility of mixing two or elements was explored, thereby developing alloys The effect of alloying elements on the metal properties was further studied extensively. For example, one of the important discoveries of Bronze age was tin. This metal held significance due to its ability to form an alloy with copper, i.e., Bronze. The use of tin in varying quantities in the alloy and the subsequent improvement in material properties and microstructure was further studied. This period was followed by the Iron Age lasting from 1500 – 500 B.C. [16]

The period between 200 - 500 A.D, led to the development of steel as an alloy of Iron. This resulted in vast applications of steel in shipbuilding, tool making, and weapon manufacturing, due to its high strength. During 1500-1900 A.D, metals such as Aluminum and Titanium were discovered and quickly attracted attention due to their properties such as high strength, low density, and resistance to corrosion [17].

Metals discovered after 1800 such as chromium, beryllium, vanadium, etc. have huge commercial importance, owing to their application as alloying elements in order to improve the chemical, mechanical and electrical properties of most metals [16].

To achieve superior performance and improved lifespan, applications demanded materials with excellent physical, chemical and mechanical properties. In this quest for materials with superior properties, Iron, Titanium, Nickel and other Super-alloys found applications in several challenging areas. Furthermore, ceramics, composites, polymers, CNT and other nanomaterials were also extensively developed for their thermal, mechanical and anti-corrosive properties. These materials exhibit excellent thermal and mechanical properties, along with appreciable corrosion resistance and are therefore employed for industrial and automotive applications, to cater to the growing demands of durability, strength, and cost optimization [17]. In this regard, a new class of materials was discovered in 1960 known as Metallic glass, revolutionized the field of material science. These metallic glasses (MGs) exhibit superior strength (often 3 times that of conventional metals) and excellent wear and corrosion resistance. This allowed for their application in various industries ranging from medical to aerospace.[5]

This thesis discusses metallic glasses, properties, and potential processing techniques that can be employed. Due to limitations in conventional processing methods, alternative methods such as laser deposition, powder consolidation, etc. were explored [18, 19]. Of these, spark plasma sintering (SPS) has gained significance lately and is employed to manufacture these metallic glasses in the present study. Additionally, the use of SPS to manufacture metallic glass composites and coatings is also explored in this current study. The wear and corrosion resistance of the sintered discs are evaluated to assess their potential engineering application.

1.1.2 Bulk metallic glasses

Metallic glasses/amorphous alloys are a novel class of materials that exhibit a disordered atomic structure (represented in Fig.1) contrary to that seen in polycrystalline materials. These alloys are

prepared by heating the metal to its liquidus temperature and sufficiently undercooling it using high cooling rates, sometimes of the order of 10^6 K/s [20]. This allows the freezing of the molten liquid in its solid form without crystallization, thereby giving rise to a metal with disordered random structure, known as the amorphous alloy or metallic glass. Due to this lack of ordering, these alloys absorb less energy upon deformation. The absence of a crystalline arrangement removes the possibility of structural defects, leading to high strength, hardness, toughness, and elasticity. All compositions of metallic glasses adhere to three simple rules of mixing, which are aimed at preserving the amorphous nature of the alloys. They are:

a) The size difference between the constituent elements must be greater than 12%;

b) All components in the alloy must have a negative heat of mixing;

c) There must be three or more elements and the alloy composition must be as close to the eutectic liquid as possible to facilitate glass formation at low temperatures [20].

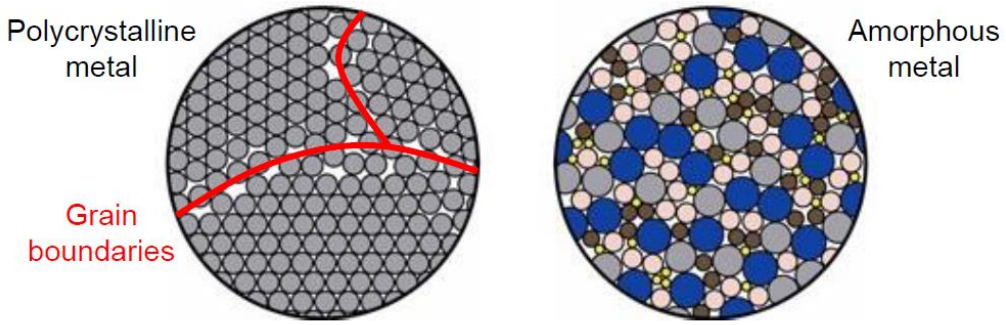

Fig. 1 Schematic representation of the atomic structure of (a) Polycrystalline metal, and (b) amorphous metal [1].

The absence of grain boundaries in metallic glasses contributes to their wear and corrosion resistance. However, the need for high critical cooling rates to preserve this amorphous structure has restricted the size and variation in the structures formed to ribbons, powders, and films,

processed using rapid solidification techniques such as melt quenching and die casting. This resulted in metallic glasses being produced as just wires and thin films.

Most metallic glasses although possess high strength, are extremely brittle in nature. They undergo sudden failure that is often catastrophic, therefore limiting the use of MGs in structural applications. The structural deformation in MGs at room temperature takes place in the form of highly localized shear bands. There are two micro-mechanisms that contribute to the deformation in MGs- free volume dilatation and shear transformation zones (STZ). The STZs are areas that have localized concentration of shear bands and range from 2.5 to 6.6 nm^3 in size [5].

To overcome the brittleness and poor ductility of these metallic glasses, metallic glass composites have been developed. These composites consist of an amorphous matrix that is reinforced with crystalline phase or amorphous phase. This, in turn, can contribute to the improved wear behavior and mechanical properties. However, excessive addition of these reinforcements can make the amorphous matrix more brittle than the original metallic glass and further deteriorate the wear rate[21]. Due to the limitation put forth by high critical cooling rates restricting the size of the metallic glasses, alternate methods to utilize metallic glasses as coating materials are being explored. Various thermal spray technologies and electrodeposition methods were used to successfully coat metallic glass on crystalline substrates to improve their surface characteristics. Although these coatings improved the wear and surface properties of the crystalline alloy, most of these coatings were highly porous and only a few micrometers thick.

1.1.3 Spark plasma sintering

SPS is a new approach that makes use of simultaneous application of electric currents and uniaxial pressure to consolidate powders. SPS offers advantages such as the use of relatively high heating rates over conventional sintering that allows processing of metallic glass below their glass transition temperature.

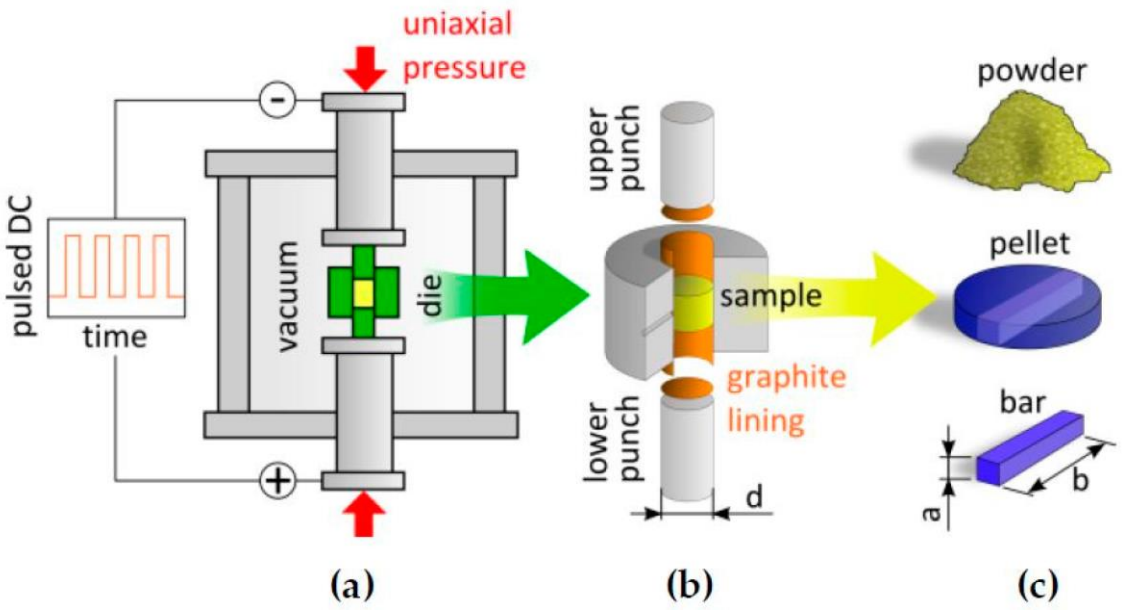

Fig. 2 Schematic of (a) Experimental set-up of spark plasma sintering, (b) die-punch arrangement, and (c) raw material used and final product obtained [3]. (Image Reprinted with Permission from Springer).

The setup consists of powders placed at the center of a graphite die. The die is compressed from both ends using a hydraulic press. The use of graphite dies limits the maximum pressure applied to 100 MPa. To obtain higher pressure, WC dies can be employed. The temperature of the powder is raised by means of pulsed DC current. This results in Joule heating, which is utilized to obtain the desired temperature. Further, the graphite die ensures uniform electrical conduction in the powder from all sides. With the application of electric current. localized heating takes place on the surface of these particles. This localized heating can produce very high temperatures similar to those generated at the core of plasma due to ionized gasses between particles, therefore giving this process its name of spark plasma sintering [22]. However, the occurrence of this spark is widely debatable and has led to the process being referred to as field assisted sintering technique (FAST) or pulsed electric current sintering (PECS).

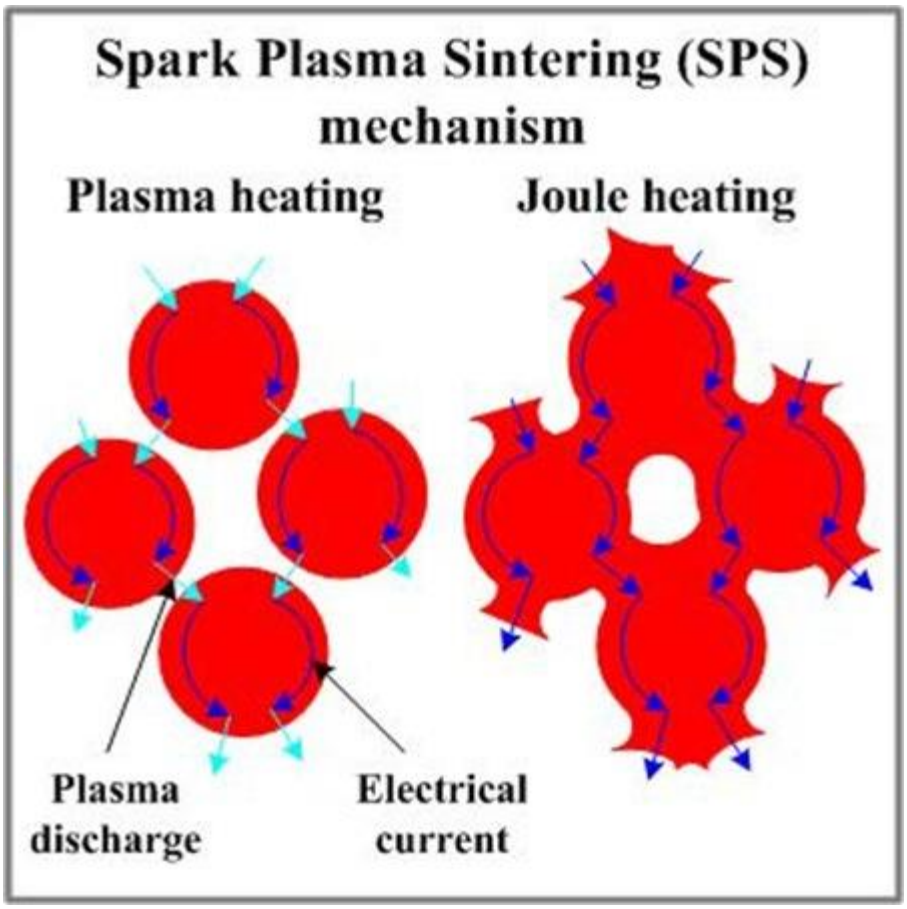

Fig. 3 Densification process and neck formation during sintering [2]. (Image Reprinted with Permission from Springer).

Rapid heating can bypass the low-temperature region where sintering is dominated by surface transport. Mass transfer on the surface of the powders takes place by means of diffusion. This plays an important role in the densification of the alloy. Densification of the powder compact takes place during the heating of the particles as represented by the mechanism in Fig. 3. The powders undergo Joule heating, wherein the current travels across a path of least resistance, offered by the contact points between adjacent particles. The electric discharges on the surface produce a cleaning effect, by eliminating any oxide layers or impurities absorbed by the powders. Simultaneous application of mechanical compression leads to compaction and deformation of the

powders. This results in diffusion bonding. The initial stage of sintering results in compacts with high porosity. As temperature increases, the rate at which grain boundaries diffuses increases. As the activation energy for surface diffusion is low during the initial stages, mass transfer takes place in this mode, instead of other mechanisms. It was also found that densification rate is high during initials stages of sintering, leading to complete densification at lower temperatures [23-25]. The mass flow follows a path along the boundary and tends to get concentrated at the point of contact between the particles. Although the pores exhibit a pinning effect initially, this contributes to arresting the grain size of the compact at the final stage [26]. Further, the applied pressure during sintering was found to be amplified at the point of contact between powder particles, thereby contributing to enhanced densification of the compacts. Therefore, pressure and temperature simultaneously contribute towards sintering in very low cycles, producing compacts with near complete density of that of the alloy [27]. The mechanism of sintering can be precisely understood using Johnson-Mehl-Avrami-Kolmogorov theoretical framework and the rate of densification can also be predicted in the viscous flow regime of powders [28].

In the case of metallic glasses, SPS offers the advantage of processing metallic glasses at low temperatures typically below the glass transition temperature of the alloy. This allows the retention of the amorphous phase to the maximum extent possible. In addition, SPS allows sintering of compact discs with a density similar to that of the as-cast alloy. Although the sintered discs possess mechanical properties on par with the as-cast alloy, the tribological and corrosion resistance needs to be evaluated for their use in engineering applications.

1.1.4 Wear

Wear is defined as ‘damage or deformation of surfaces that results in eventual loss of material’. Mechanical loading, moving components, fatigue failure, and loss of vibrational damping are some causes of friction that result in wear of materials. Although the wear of surfaces can be effectively controlled by sufficient lubrication, gradual depletion of lubricants must also be

considered to prevent excessive wear. Based on the interaction between two surfaces, two body wear or three body wear can take place. Some of the most common types of wear found in materials are sliding, rolling and impact wear schematically represented in Fig. 4. These can be explained by different wear mechanisms such as abrasion, adhesion, tribo-chemical, oxidative, and erosive wear to name a few. Wear is a complex phenomenon that often involves one or more mechanism. These different types of wear are further discussed in detail [29].

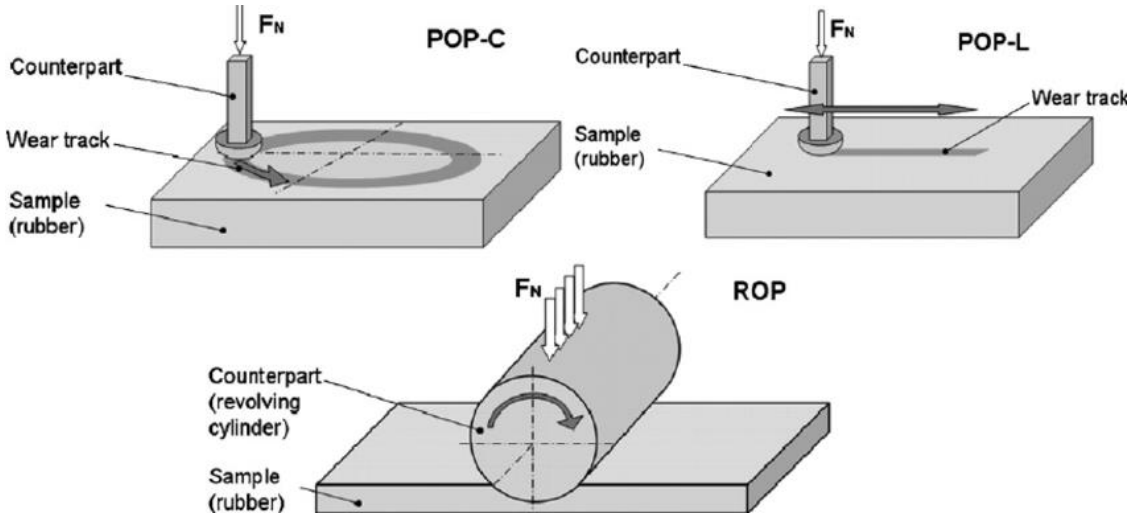

Fig. 4 Experimental set-up of various types of wear test rigs [3]. (Image reprinted with permission from ELSEVIER)

Sliding wear often results between interacting surfaces that are in relative motion with each other. As surfaces interact, sliding wear occurs and can take place with or without lubrication. In the presence of lubrication, lubricated wear takes place whereas, without lubrication, dry sliding wear takes place. However, in the presence of a hard particle between the surfaces or in the surface topography of one of the materials, may result in abrasion causing more wear. During wear, the debris generated can lead to abrasion of surfaces thereby resulting in accelerated wear loss and increased wear. This can result in abrasive wear of the material. Adhesive wear occurs due to the transfer of material from one surface to the other. It is characterized by high wear loss and

unstable coefficient of friction [29]. Plastic shearing of successive layers of materials is a common observation during wear. Propagation of shear cracks underneath the surfaces has also been observed that eventually results in delamination of material. The mechanical interaction between the surfaces plays a major role in this type of wear mechanism. On the other hand, thermal reactions on the surface result in oxidative wear, which involves the formation of a protective oxide tribo-layer due to localized surface heating. Although the oxide film contributes to reducing wear, the eventual breakdown of the film further increases wear due to abrasion of the surface by the oxide particles released from the film. The wear mechanism is governed by the Archard's wear equation that correlates wear coefficient (K) with the normal load applied (W), sliding distance, volume wear loss (Q), and hardness of the material (H) [30].

$$Q = \frac{KW}{H} \ldots\ldots\ldots\ldots\ldots\ldots \quad (1)$$

The damage on the surface due to wear is described in terms of scuffing, scoring, galling, plowing etc. Scuffing is used to refer to localized wear that is often associated with solid-state welding of particles on the surface. It is also referred to a breakdown in lubrication that results in localized wear. Scoring although synonymous with scuffing describes scratching of surfaces by abrasive particles. Galling is used to describe surface damage occurring in large scales. This can be a direct result of low sliding speeds on roughened surfaces marked by displacement of the large volume of material across surfaces [29].

Although the above theory can be used to explain wear in most conventional metals, wear in metallic glasses takes place in two stages. The initial stage is called the running-in stage where the material loss is either high or low. This is due to the initial interaction between the counter-body and the test sample. As the test progresses, a steady-state is achieved where the material loss decreases with sliding distance and eventually stabilizes. However, inclusions during solidification or presence of hard particles in the matrix have found to significantly affect the

wear behavior of these metallic glasses. Crystallization of wear debris with prolonged sliding distances and re-amorphization of this debris was also reported. Formation of a protective oxide layer, due to localized heating during wear tests is also reported as a common observation [21].

1.1.5 Corrosion

The corrosion resistance of a metal can be explained as the electrochemical response of a metal in a highly conductive medium. The reaction takes place between an anode and a cathode, where oxidation occurs at the anode and reduction occurs at the cathode. This oxidation thereby leads to corrosion of the anode. Various forms of corrosion have been identified based on the reaction between the metal and the surrounding media. Of these, pitting, crevice corrosion, dealloying, stress corrosion cracking are some common forms found in most engineering applications [31]. The corrosion resistance and corrosion behavior of the material are evaluated using tests such as immersion corrosion, salt spray, and salt fog, and potentiodynamic tests to name a few. Cyclic polarization testing can be effectively used to study the corrosion behavior of a metal in an active corrosion media. These cyclic polarization tests have been used to study localized corrosion of metals, due to both anodic and cathodic polarization mostly. This can be studied using their polarization potentials. These tests are conducted on a measured area of the sample that is exposed to the corrosion media. The potentials plotted against current density result in a cyclic loop [32].

The cyclic plot of the cyclic polarization tests is plotted as seen in Fig. 5. These plots sometimes show evidence of anodic polarization displayed in the figure, marked by the constant increase of the anodic potential to a certain value. In such cases, this region can be termed as the passive region. The sudden increase in potential could be a result of various chemical and environmental factors or possibly indicate the development of a protective film on the surface constituting corrosion products. After a certain time, the potential stabilizes where the plot transcends into a trans-passive region. The transition between the passive and trans-passive the region is marked by

breakdown potential (E_{bd}). The curve eventually records negative potential tracing the curve back to its corrosion potential region, thereby completing the cycle [33].

In the case of metallic glasses, their superior corrosion resistance is primarily attributed to their atomic arrangement. However, in some alloys, the composition was also found to significantly influence the corrosion behavior of the metallic glass. The presence of elements such as Ta, Cr, Mo etc. that are susceptible to forming a protective oxide layer improved the corrosion resistance of metallic glasses [12, 14, 34]. This property of the metallic glasses is further explored and discussed in detail in the following sections.

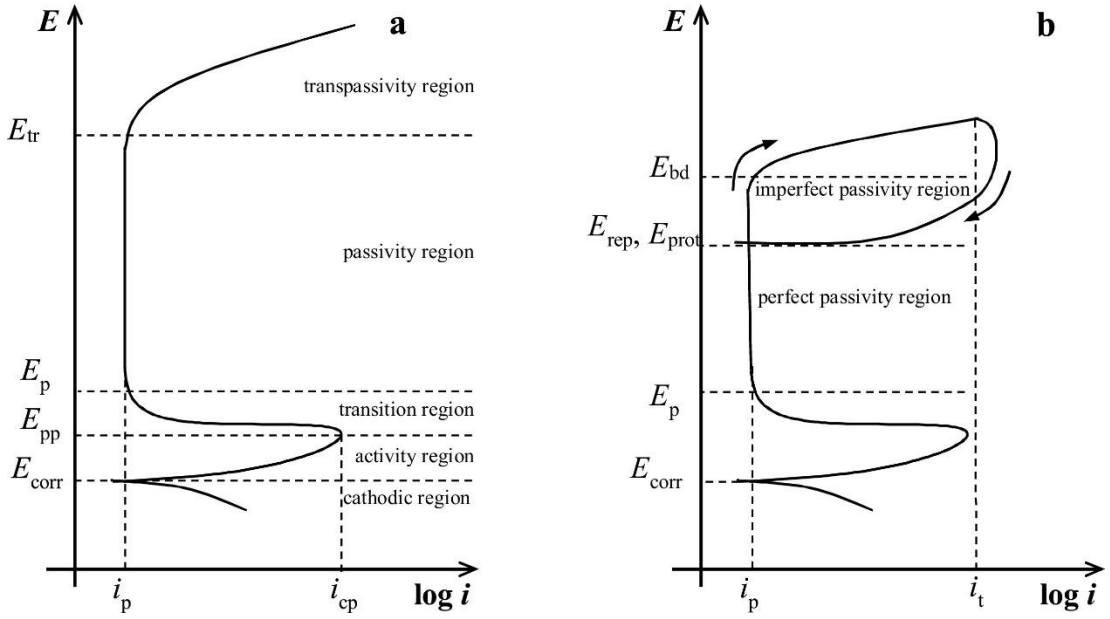

Fig. 5 Potentiodynamic polarization curves representing (a) passive and transpassive regions, and (b) cyclic polarization curves [4]. (Image reprinted with permission from ELSEVIER)

.

1.2 Literature Review

The first metallic glass was discovered in 1960 at Caltech, by Dr. Johnson and his research group. A binary metallic alloy $Au_{80}Si_{20}$ was rapidly quenched using 10^6 K/sec, resulting in the formation of opaque, gray, shiny and smooth metal solidified at its glass transition temperature. Due to this, the metal is brittle, although less than oxide glass. Among the many metallic glass alloys developed Zr-, Pd-, Ti-, Ni, Fe-, Ni-based metallic glasses are a few that were widely popular due to their ease of glass formation and properties such as high strength, hardness, toughness, superior wear and corrosion resistance to name a few.

1.2.1 Zr-based metallic glass alloys and composites

Zr-based metallic glass with composition $Zr_{41.2}Ti_{13.8}Ni_{10}Cu_{12.5}Be_{22.5}$ known as Vitreloy 1, exhibits excellent glass forming ability with a viscosity of 100 poise and a fragility index of 18.5. This alloy possesses a supercooled liquid region of 135K, which allows its casting in various sizes and shapes. Due to this, this alloy has found applications as implants, Golf club heads, electronic casing and sensors as displayed in Fig. 6. This resulted in reduced crystal nucleation and growth, due to the reduced atomic arrangement in the undercooled liquid region between T_g and T_L, which in turn allowed the alloy to be cast into parts utilized for commercial equipment such as golf clubs, metal pipes, and nets [5]. In addition, a study of the tribological properties of this material revealed that these materials display a low coefficient of friction under dry sliding conditions. The wear surface mostly exhibited inhomogeneous plastic deformation with abrasive, adhesive and oxidative wear resulting in micro-cutting and peeling off [26]. The metallic glass when tested in both dry and wet sliding conditions exhibited the lowest wear rate for dry sliding while recording the highest wear rate for tests run with 30 % hydrogen peroxide as a lubricant. Adhesive wear was observed with the transfer of material from sliding disc to metallic glass alloy, with metallic glass tested during lubricated wear recording a positive weight loss. This is a typical indication of oxidative wear, with the formation of an oxide layer on the surface of the

metallic glasses. The wear mechanism was observed to change from plastic deformation, indicating abrasive wear for dry

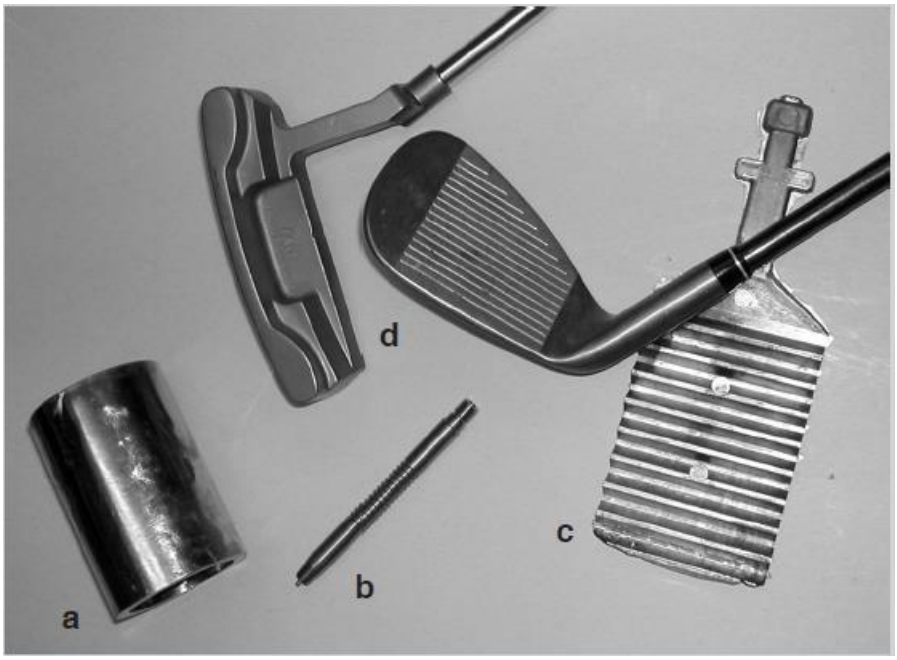

Fig 6 Vitreloy 1 bulk amorphous metal used to fabricate (a) metal pipe, (b) tungsten reinforced metal amorphous composite rod, (c) cast into net shape, and (d) golf club [5]. (Image Reprinted with Permission from Springer).

sliding conditions to a mixture of abrasive and oxidative wear resulting in peeling off of surfaces for lubricated sliding conditions

The crystallization, mechanical properties and glass forming ability of $Zr_{52.25}Cu_{28.5}Ni_{4.75}Al_{9.5}Ta_5$ metallic glass were studied by adding Ta (5 at %) to $Zr_{55}Cu_{30}Ni_5Al_{10}$ alloy. The addition of 3.2 % Ta resulted in the improved thermal stability of the alloy by increasing the glass transition temperature and crystallization temperature by 20 K. However, the T_g/T_m did not change significantly. Furthermore, with an increase in the size of the as-cast samples, it was observed that Ta induced a composition segregation layer around the particles leading to the increased precipitation of Zr_2Cu during solidification resulting in reduced ductility. Also, when the

compression behavior of the alloy with Ta was analyzed, it was observed that the fracture plane has an angle of 31–33° when compared to 42–43° for that of the original metallic glass as seen in Fig.7 [6].

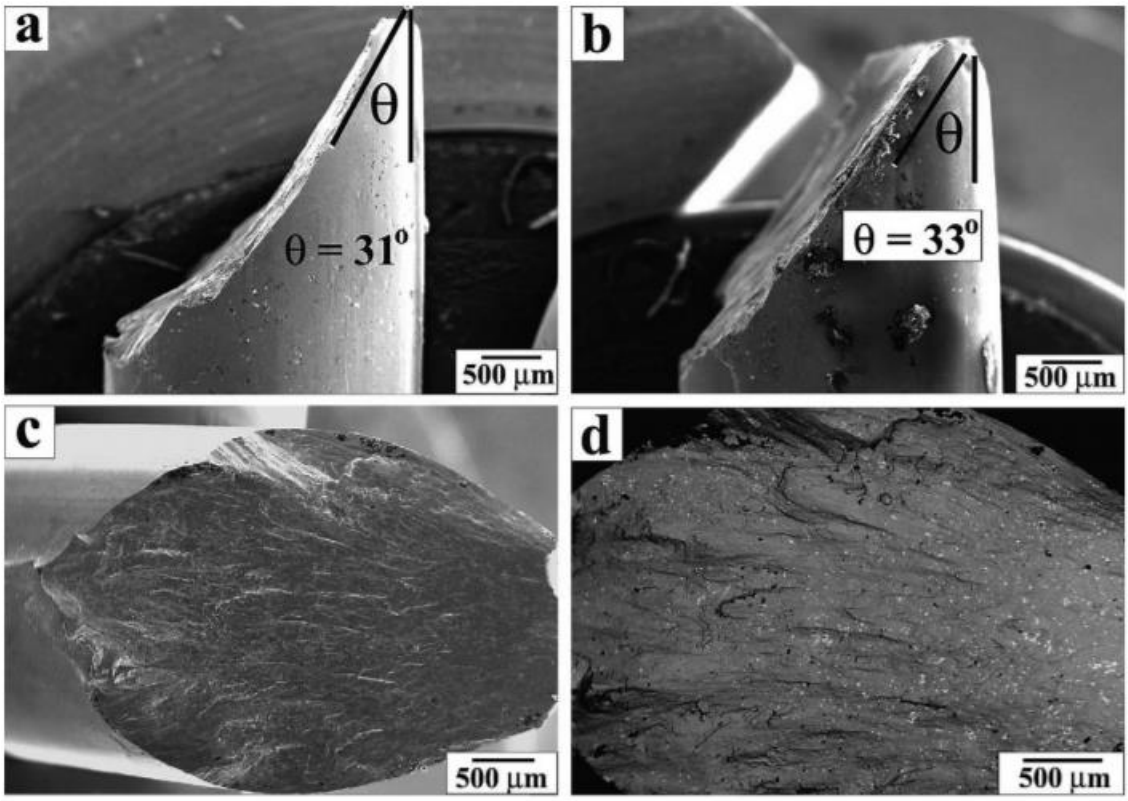

Fig. 7 SEM micrographs of the $Zr_{52.25}Cu_{28.5}Ni_{4.75}Al_{9.5}Ta_5$ alloy after compressive loading (a, b) angle of shear fracture failure during compression, and (c, d) fracture surface showing the homogeneous distribution of Ta particles [6]. (Image reprinted with permission from ELSEVIER)

The deformation of metallic glasses is through shear band propagation. The formation of these shear bands is considered a result of the degraded stress-bearing capacity of the material with an increase in plastic strain. These internal strains can be produced due to tension, bending or torsion. The study of this shear band propagation was carried out with stress being applied in different directions. It was observed that the spacing and orientation of these shear bands were largely dependent on the mode and plane of stress created. Certain shear bands exhibited

multiaxial stress fields that in turn resulted in the creation of secondary shear bands [35]. To restrict the propagation of these shear bands, in situ or reinforced bulk metallic composites have been developed.

A possible example of metallic composites would be the that of CNT distributed in a matrix of $Zr_{52.5}Cu_{17.9}Ni_{14.6}Al_{10}Ti_5$. The CNT powder was homogenously distributed and resulted in the formation of a ZrC indicating reaction between the CNT and metallic glass matrix. Although the glass transition temperature did not change, the onset of crystallization shifted to a slightly higher temperature, indicating that composite with CNT has a different crystallization behavior. The composite recorded higher viscosity, elastic modulus and hardness due to the addition of CNT. A marked decrease in density allows the composite to be used in manufacturing lightweight materials [36]. A two-phase metallic glass with composition $Zr_{63.8}Ni_{16.2}Cu_{15}Al_5$ (in at. %) was tested in compression. Micropillars of 3.8,1 and 0.7 μm were fabricated and tested in compression using strain rates of 10^{-4} to 10^{-2} s^{-1}. The yield strength of these micropillars was recorded to be 1992–2972 MPa, approximately 1600 MPa higher than that of the bulk samples. It was deduced that as the size of the sample decreases, the defect population reduces thereby increasing the strength of the metallic glass [37].

Another $Zr_{48.5}Cu_{46.5}Al_5$ bulk metallic glass composite was prepared by reinforcing the matrix with martensite plate and other phases such as nanocrystalline Zr_2Cu and plate-like $Cu_{10}Zr_7$ compounds. Compression tests performed on these samples displayed a yield strength of 1640 MPa with a plastic deformation of 6.4 %. Analysis of fracture surface has resulted in shear bands oriented at an angle of 45° to the shear plane. It was deduced that the micrometer-sized CuZr phase underwent strain hardening, preventing shear band propagation as seen in Fig. 8(d) and thereby improved plasticity [7]

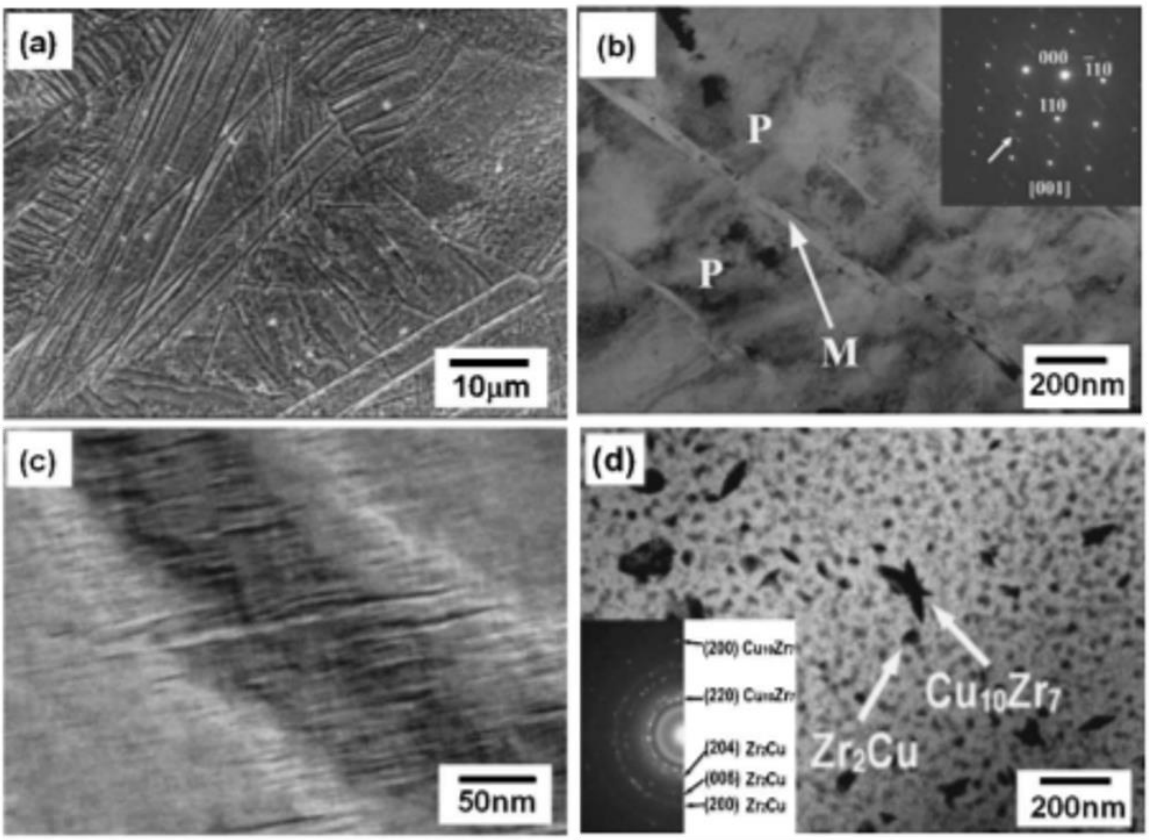

Fig. 8 Micrographs of metallic glass samples exhibiting (a) martensitic structure in SEM image; (b) parent phase and martensitic phase, (c) micro-twins, and (d) crystalline phases distributed in the amorphous matrix as seen from TEM images [7]. (Image reprinted with permission from American Institute of Physics (AIP)).

1.2.2 Ti-based metallic glass alloys and composites

Ti-based metallic glasses were extensively developed due to their excellent strength and corrosion resistance. The alloy with composition $Ti_{65-x}Zr_xBe_{18}Cu_9Ni_8$ (x=10 to 15) was successfully cast into cylinders of diameter up to 6mm using injection casting. As the Zr content increased, the glass forming ability of the alloy improved due to a significant difference in atomic size between Zr and other constituent elements. In addition, alloys with greater than 50 % Ti recorded high specific strength along with high Vickers hardness in the range of 600-700. [38].

Most Ti-based metallic glass alloys have exhibited high strength, low elastic modulus, and good corrosion resistance. With studies focused on improving the GFA of these alloys, Ti-based metallic glassess and metallic glass composites can be widely used as biomedical devices and implants. Numerous studies have shown that addition of elements such as Sn and Be has not only improved the tensile strength of the alloys but has also increased the critical diameter for the bulk alloy with a single amorphous phase. In addition, Sn was found to improve the glass forming ability of Ti-based metallic glasses and thereby significantly affecting its crystallization behavior by forming icosahedral nanocrystals. However, the presence of Ni, Be, and Al in these alloys makes it impossible to use these alloys as potential materials for bioimplants, due to their detrimental effect on the human body.

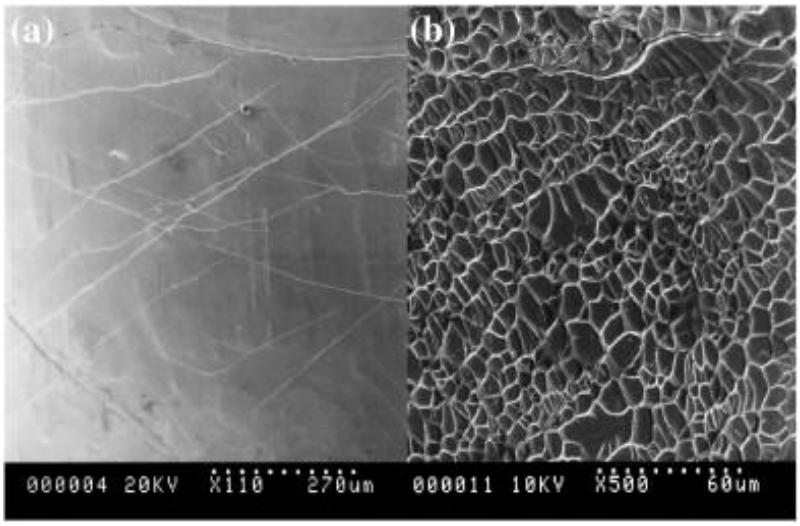

Fig. 9 The fracture surface of $Ti_{44.1}Zr_{9.8}Pd_{9.8}Cu_{30.38}Sn_{3.92}Nb_2$ alloy under compression exhibiting (a) crack propagation with shear bands, and (b) vein patterns [8]. (Image reprinted with permission from ELSEVIER)

Alloy ingots with composition $(Ti_{0.45}Zr_{0.1}Pd_{0.1}Cu_{0.31}Sn_{0.4})_{100-x}M_x$ (at. %)(M: Ta and Nb, x = 1, 2, 3, 4, 5) were prepared. Ribbons and cylindrical samples were prepared by copper mold casting. These alloys exhibited good thermal stability and large supercooled liquid regions indicating

good glass forming ability. In particular, $Ti_{44.1}Zr_{9.8}Pd_{9.8}Cu_{30.38}Sn_{3.92}Nb_2$ alloy exhibited excellent GFA and a critical rod diameter of 5mm. The compressive strength of this alloy resulted to be 1990 MPa, higher than conventional crystalline Ti alloys or Ti–6Al–4V alloy. The failure of the

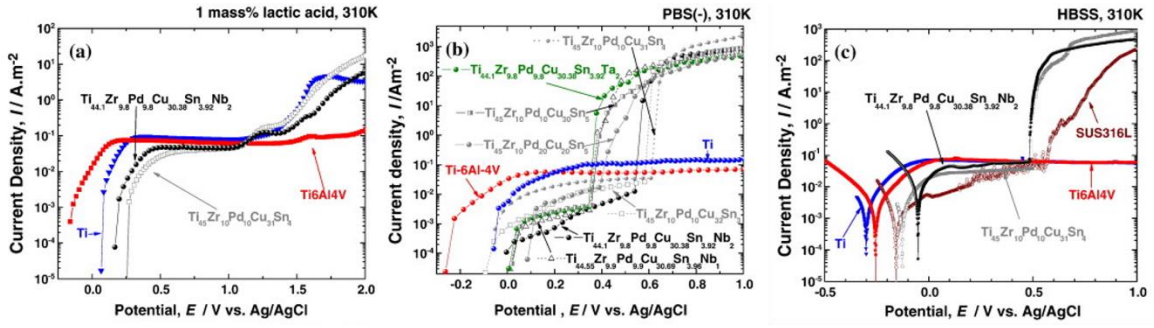

Fig. 10 $Ti_{44.1}Zr_{9.8}Pd_{9.8}Cu_{30.38}Sn_{3.92}Nb_2$ alloy exhibiting anodic polarization in 1 mass% lactic acid electrolyte: (a) phosphate-buffered saline without calcium and magnesium salts solution, (b) Hank's balanced salt solution without calcium, magnesium, and phenol red, and (c) in solutions open to air at 310 K [8]. (Image reprinted with permission from ELSEVIER)

the alloy is due to shear band propagation as seen in Fig.9.The formation of vein-like patterns on the fracture surface indicates the ductile behavior of the alloy during compression. The alloy also exhibits high corrosion resistance with a wide range of passivity. The current densities of the alloy was approximately 10^{-2} A m^{-2} in 1 mass% lactic acid, 10^{-3} A m^{-2} in PBS(−) and 10^{-2} A m^{-2} in HBSS aqueous solutions open to air, which was lower than Ti and Ti-6Al-4V alloy as seen in Fig.10 making it an ideal material to be used in dental implants [8]

The failure analysis of these Ti-based metallic glasses, when tested in cryogenic temperatures revealed that by decreasing the test temperature, shear band propagation can be controlled and branching of shear bands can take place during fracture. This can result in the improved plasticity of the metallic glass, thereby promoting opportunities for application of these metallic glasses as high-performance structural materials. DSC studies revealed that during plastic deformation

atomic dilation occurs due to the localization of plastic strain. As a large portion of atoms will be mobilized, local displacements will enhance this diffusion and atomic mobility thereby promoting crystallization. In addition, localized heating within shear bands was observed during plastic deformation, leading to crystallization in areas surrounding the shear bands. Therefore, testing or use of these materials in low-temperature surroundings, suppresses growth and propagation of these crystalline phases, resulting in improved plasticity and enhanced strength [39].

Although most Ti-based metallic glasses have exhibited good corrosion resistance, not all alloys can resist pitting, therefore restricting the use of these alloys as potential biomedical applicants. Ti-based metallic glass with composition $Ti_{43.3}Zr_{21.7}Ni_{7.5}Be_{27.5}$ (at.%) was tested in phosphate-buffered saline solution with a dissolved oxygen content of physiological relevance. The alloy exhibited passive open circuit potential behavior with a relatively low mean corrosion penetration rate that was comparable to 316L and metallic glass of other composition. The samples exhibited many microscopic pits scattered on the surface in addition to large pits. The location of these pits was associated with the inhomogeneous amorphous matrix. In addition, microstructural inhomogeneities incorporated during casting, such as voids or heterogeneous impurities incorporated such as oxides also promote severe pitting of the surface.

The stable passive film formed on the surface also breaks down due to defects, resulting in penetration of the film due to severe chloride ion attack [40]. However, most metallic glasses exhibit superior corrosion resistance due to their inhomogeneous structure. Also, the formation of a protective surface film was observed in most studies, resulting in enhanced protection from corrosion of these composites. Electrochemical studies of $Ti_{45}Zr_{10}Pd_{10}Cu_{31}Sn_4$ metallic alloy exhibited high corrosion resistance after immersion in 3 mass % NaCl, 1 N H_2SO_4, and 1 N H_2SO_4 + 0.01 N NaCl solutions. The single phase chemically homogenous structure was attributed to the superior corrosion resistance of the alloy. XPS studies performed on the immersed samples have recorded the presence of a highly protective surface film that is rich in Ti

and Zr ions. The performance of the alloy was compared after immersion in NaCl and HCl solutions. Although both solutions were rich in Cl ions, the dissolution of the alloy was severe in HCl solution when compared to the other. This was credited to the stability of the surface film formed and its constituents.

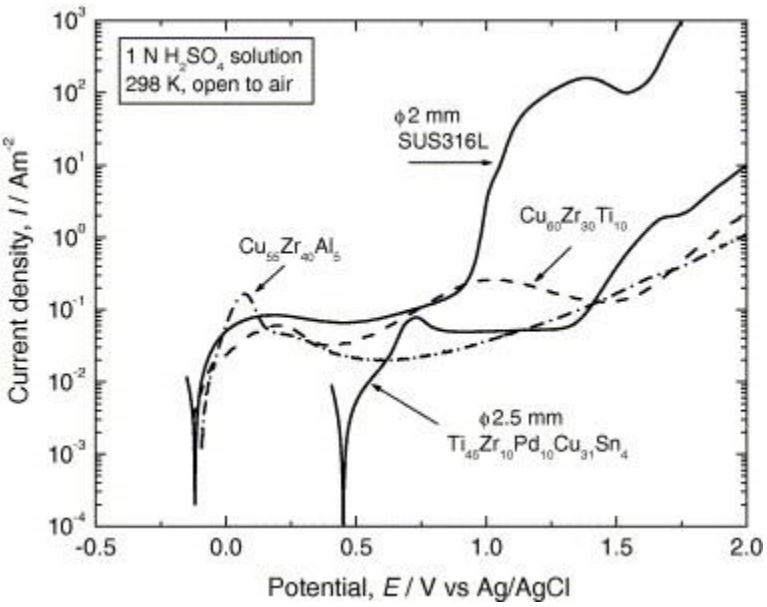

Fig. 11 Corrosion behavior of $Ti_{45}Zr_{10}Pd_{10}Cu_{31}Sn_4$ alloy in different electrolyte solutions, compared with other metallic glasses [9]. (Image reprinted with permission from ELSEVIER)

The presence of Cu cations in the surface film has led to poor stability of the protective film formed and thereby causing excessive alloy dissolution in HCl solution as seen in Fig. 11. It was also observed that accumulation of non-protective corrosion products on the surface of the film can lead to increased thickness of the film albeit degraded corrosion resistance. Therefore, for the alloy to have superior corrosion resistance, the thickness and concentration of the surface film formed to play a major role [9].

Ti-based metallic glass composites reinforced with a crystalline phase have shown improved mechanical properties. However, excessive addition of crystalline phase has resulted in increased brittleness of the matrix. $Ti_{40}Zr_{29}Cu_8Ni_7Be_{16}$ alloy was reinforced with in situ quasicrystals produced by annealing. The size of these quasicrystalline precipitates was 5-10 nm and was homogeneously distributed throughout the matrix Mechanical properties of these composites were evaluated using compression tests and compared with that of the as-cast alloy. The yield strength and global strain of the annealed composite were 2038 MPa and 6.2% while that of the as-cast alloy was 1893MPa and 5.1%. By the precipitation of these icosahedral quasicrystals, the hardness of the composites was also found to improve. However, with an increase in the volume fraction of these crystals beyond 7%, the plastic strain of the composite decreased. As the shear deformation of these metallic glasses takes place by localized shear band formation, a simultaneous increase in strength and global strain of the partially crystalline alloy can be related to the formation of shear bands. However, the quasicrystals can act as both sites of nucleation as well as barriers for shear band propagation. But due to the negligible difference in size between the amorphous phase and the quasicrystalline phase, the interface between the two displays a dense atomic configuration along with a gradual transition between the amorphous and quasicrystalline structure devoid of unwarranted vacancies. This stability of the interface prevents shear band propagation, encouraging branching of multiple shear bands generated thereby improving the strength and ductility [41].

Furthermore, it has been reported that the size of these reinforcements and their dispersion also play a major role in the plastic deformation of the composites. The presence of dendritic reinforcements that are few micrometers in size throughout the alloy has resulted in perturbances along these shear bands. The shearing off of these shear bands was successfully prevented by the crystalline reinforcements in the dendritic phase, providing significant work

hardening and thereby resulting in the homogeneous deformation of the alloy. The ductility of these composites was improved by nearly 6% plastic strain before failure [42].

1.2.3 Ni-based metallic glass alloys and composites

The foremost concern of any metallic glass alloy is to obtain high glass forming ability by achieving as high an undercooled liquid region as possible. The NiTiZr alloy was modified by adding small amounts of Sn and Si, replacing Ti. For the $Ni_{57}Ti_{23-x}Zr_{20}(Si, Sn)_x$ alloy it was found that with the addition of Sn by 5 %, the glass forming ability of the ability of the alloy increased by 33 K due to the variation of T_g and T_x as seen in Fig. 12. This was observed to be a result of the large atomic size of Sn atoms that disrupt phase formation. However, with further additions of Si, the GFA was found to increase to as high as 50 K. This was due to the negative heat of mixing between Si and Ni. It was also reported that T_g of the alloy increased with the addition of Si due to the strong bonds formed between Si and its constituent elements. However, the change in T_x was the only nominal with the addition of Si beyond 5 %. Furthermore, the $Ni_{57}Ti_{18}Zr_{20}Si_5$ alloy had the lowest liquidus temperature, making the liquid phase of the alloy relatively stable. This allowed the alloy to be undercooled to much lower temperatures using relatively low cooling rates when compared with other alloys. This allowed the fabrication of amorphous rods of 2 mm in diameter using copper mold casting. Also, the heat treatment of these rods in the undercooled region improves the viscosity of these alloys and allows them to be shaped by injection molding [10].

The Ni–Nb-Ti–Zr system also reported a 51 K of the undercooled liquid region with the addition of Co and Cu. Although this is in accordance with other Ni-Ti-Zr alloy systems, this alloy

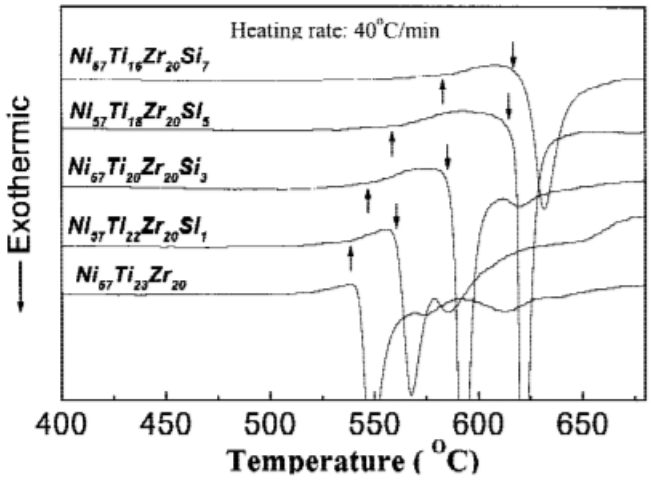

Fig. 12 Variation in T_g and T_x with Si content in the Ni-based metallic glass as displayed in DSC analysis [10]. (Image reprinted with permission from Cambridge University Press).

exhibited excellent mechanical properties during tensile and compression tests. The tensile fracture strength was 2700 MPa, Young's modulus of 140 GPa and elongation in tension was 2.1%. The compression tests reported compressive fracture strength of 3010 MPa and elastic elongation of 2.4%. The tensile fracture strength was believed to be highest for all metallic glasses reported to date. The tensile fracture strength of this alloy was investigated as a factor of T_g or T_m. As T_g or T_m is majorly influenced by the bonding forces of the constituent elements, it is believed that such high tensile fracture strengths are a direct result of the strong bonding between the elements Ni, Nb, Ti and Zr that constitute a most of the composition. The negative heats of mixing between Ni-Nb, Ni-Zr, Ni-Ti systems attest to this theory. In addition, the improved ductility of the alloy is due to the zero heat of mixing between Nb-Zr, Zr-Ti, and Nb-Ti. Also, due to the atomic size between Nb/Ni, Zr/Ni, Ti/Ni, Zr/Nb, Zr/Ti being greater than 1and atomic bonding nature , the alloy components can be credited to the exceptional glass forming ability and high strength with a balance of attractive and repulsive bonds between them. This has resulted in casting an alloy of 3 mm in diameter with copper mold casting [43].

A comparison of the abrasive wear behavior of metallic glasses with polycrystalline metals can be seen in Fig. 13. Although most metallic glasses have exhibited excellent wear resistance when compared to commercial crystalline alloys, Ni-based metallic glasses of compositions Ni91Si7B2 and $Ni_{72.5}Cr_{18.5}Si_{7.5}B_{1.5}$ reported high wear rates when tested for two-body abrasive wear characteristics. The wear tests were performed for reciprocating and uni-directional wear followed by indentation tests on the worn surface. The specific wear rate of these two alloys, when compared with that of 304 stainless steel, is relatively high. The $Ni_{91}Si_7B_2$ metallic glass displayed higher wear than the other. However, although the overall wear in stainless steel was higher at the beginning, it gradually decreased and stabilized to that of the $Ni_{91}Si_7B_2$ amorphous alloy. While SEM micrography and acoustic emission studies of worn surfaces were carried out, it was observed that most metallic glasses exhibit arc-like features that extend into grooves on the scratch surface. However, Ni-based metallic glasses displayed complete cracking of the material on the surface. The microcracks or arc-like features in most Fe based metallic glasses are attributed to the poor ductility of these alloys in tension. These features formed due to brittle fracture are comparable to those found in most ceramics. A material pileup in some areas also indicates micro cutting and micro-plowing action of the indenter. Features such as grooves, micro-cutting, and micro-plowing have also been observed in the stainless-steel sample. Inspection of scratch surfaces during tests using acoustic emission resulted in the generation of tensile micro-cracks. However, these cracks were not observed in the stainless-steel sample. It can be concluded that although metallic glasses exhibit high strength and hardness, they result in excessive two-body abrasive wear [11].

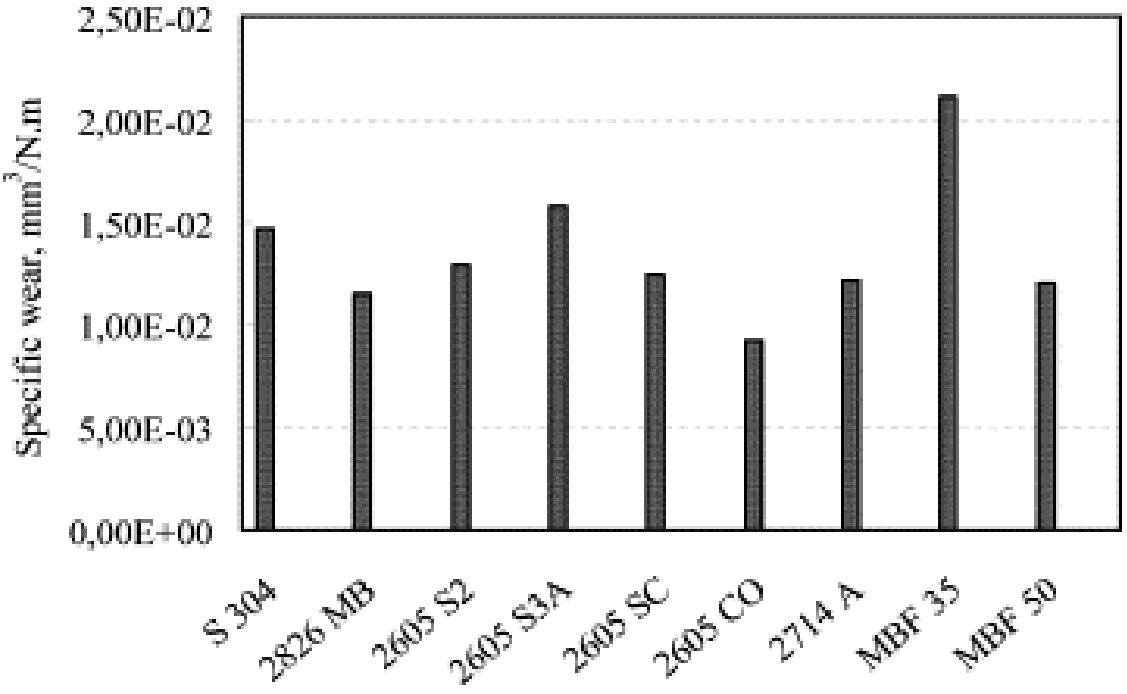

Fig. 13 Comparison of abrasive wear of various Ni-based metallic glasses with a few poly-crystalline alloys [11]. (Image reprinted with permission from ELSEVIER).

The electrochemical behavior of these Ni-based alloys resulted in low corrosion rates with these alloys displaying high corrosion resistance. Ni-Nb-Ta-P alloys in particular exhibited high corrosion resistance in particular with being immune to pitting due to anodic polarization. This was found to be due to the presence of Tantalum in the alloy composition. The cyclic polarization curves of Ni-Nb-Ta-P alloys that are 1mm and 2mm in dia, in the presence of 12 M HCl solution can be seen in Fig. 14 and Fig.15 respectively. Pure tantalum has also exhibited low corrosion rates on par with this alloy. It is interesting to note that $Ni_{-35}Nb_{-5}Ta_{)0.95}{}_{-5}P$ alloy was fully amorphous despite not exhibiting a distinct glass transition. Alloys with greater than 30 % tantalum displayed diffraction peaks associated with crystalline phases. The most common crystalline phases were found to be Ni3Nb, Ni3Ta, and NiP. The corrosion rates of the bulk alloys and melt spun ribbons were comparable to each other and extremely low. These alloys recorded the presence of a thick black colored corrosion film that may have resulted in low

corrosion rates. Further tests have resulted in the passive layer being rich in Ta, thereby improving the corrosion resistance. With even minor additions of Ta, the corrosion rates significantly decreased. However, alloys with 2 mm in diameter, containing greater than 20 % Ta and crystalline phases exhibited extremely high corrosion rates. In addition, the increase in Ta content leads to a decrease in anodic and cathodic current densities, subsequently leading to non-responsive open circuit potential. Although the passivated alloys displayed a passive current density less than that of the tantalum alloy, the cathodic current density for oxygen is higher than Ta resulting in a passive film forming on the alloy. It was concluded that Ta addition in certain amounts was necessary to improve the corrosion resistance in HCl acidic solution [12].

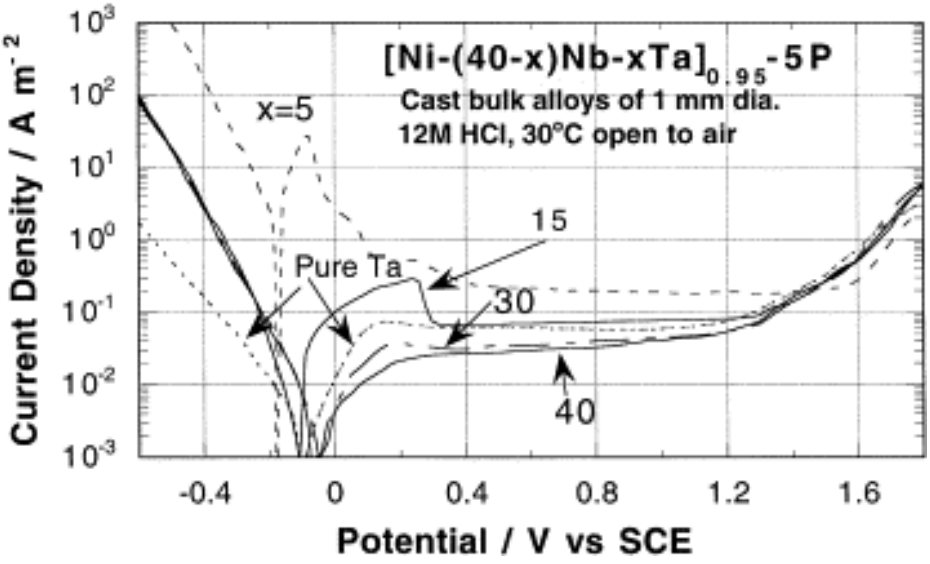

Fig. 14 Cyclic polarization curves of 1mm dia Ni-based metallic glass alloys with varying Ta content in HCl solution [12]. (Image reprinted with permission from ELSEVIER).

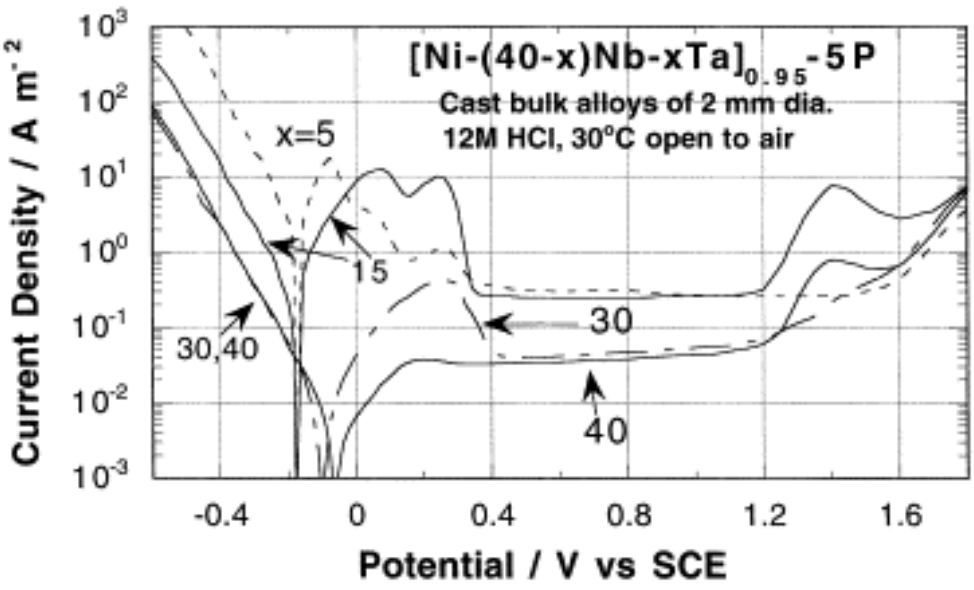

Fig. 15 Cyclic polarization curves of 2 mm dia Ni-based metallic glass alloys with varying Ta content in HCl solution [12]. (Image reprinted with permission from ELSEVIER).

1.2.4 Fe based metallic glass alloys and composites

Amorphous ribbons of composition $Fe_{77}Al_{2.14}Ga_{0.86}P_{8.4}C_5B_4Si_{2.6}$ were ball milled to produce flaky powders. These powders were cold consolidated using high-pressure torsion to produce discs with 9 mm in diameter. The Sem micrographs of the starting powders and the consolidated discs are presented in Fig. 16. It is clearly evident from the image that the alloy underwent significant strain due to torsion, that has in turn induced changes in the short-range order. This has caused the formation of nano-crystallites dispersed in the overall amorphous matrix without any signs of major crystallization. Thermomagnetic gravimeter (TMG) analysis of the ribbons and discs revealed a reduction in Curie temperature for the amorphous discs whereas an enhanced curie temperature was recorded for the ribbons. The Curie temperature was found to reduce significantly due to the crystallites formed in small sizes.

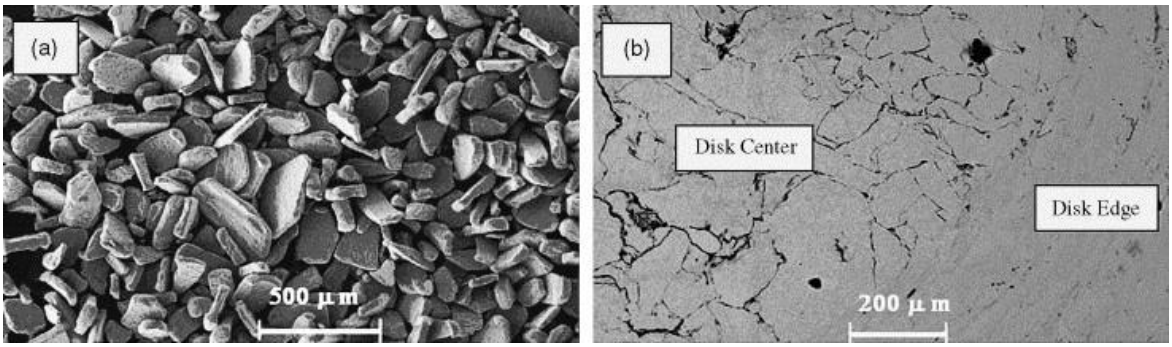

Fig. 16 Microstructure displaying (a) metallic glass powders formed after ball milling, and (b) surface of the disc fabricated using HPT [13]. (Image reprinted with permission from ELSEVIER).

It is believed that the presence of Fe_2B crystals has caused an increase in the magnetic weight of the discs beyond T>620 K. Also, these crystallites were credited to the increase in thermally induced magnetic fluctuations. The saturation magnetization of the two discs was similar with the discs recording higher coercivity than the ribbons. This increase was attributed to the structural inhomogeneities induced or the oxygen contamination during ball milling. The amorphous discs

recorded high hardness over the ribbons which can be attributed to the large amount of micro-strain along with the small amount of crystallite size in the discs as a result of the HPT process. The reduction in self-diffusion due to the high diffusion rate in the HPT process in addition to the flaky shape of the particles resulting in the dense packing of the powders may have also resulted in enhanced mechanical properties [13].

Fe based metallic alloys, in particular, have been explored as possible coatings by use of various coating techniques such as electro-spark deposition, high-velocity oxy-fuel spray, air plasma sprays to name a few. $Fe_{48}Cr_{15}Mo_{14}Gd_2C_{15}B_6$ alloy coatings were deposited on a 304 Stainless steel substrate using electro-spark deposition. The coatings were reported to be fully amorphous with a thickness of 30 μm and micro-hardness of 1540 HV. Although there was no considerable diffusion reported between the coating and the substrate, the coating was strongly bonded with the substrate without any microcracks or gaps. It is believed that the large size of Gd atom, along with negative heats of mixing between elements that constitute the alloy has favored the formation and retention of amorphous coatings with the above composition [44].

The constituent elements of Fe based metallic glasses play a prominent role in the GFA of the alloy. In some cases, these elements are also vital in improving the corrosion resistance of the alloys. For the $Fe_{69.9-x}C_{7.1}Si_{3.3}B_{5.5}P_{8.7}Cr_xMo_{2.5}Al_{2.0}Co_{1.0}$ (x = 0, 2.3, 12.3) alloy, it was found that the glass transition temperature, onset crystallization temperature increased with Cr content in the alloy. However, with an increase in Cr, ΔT_x of the alloy decreases, thereby resulting in reduced glass forming ability of the alloy. The liquidus temperature of the alloy increases with an increase in Cr content, which results in the alloy composition to move away from the eutectic composition range, thereby resulting in a decrease in GFA of the alloy. The electrochemical behavior of the alloy in 0.5 M H_2SO_4 and 1N HCl were assessed with varying Cr content. It was found that the corrosion resistance of the alloy increased with Cr content, with 12.3 % Cr in the alloy offering better resistance that austenitic stainless steel. Cr is known for forming a passivating film that

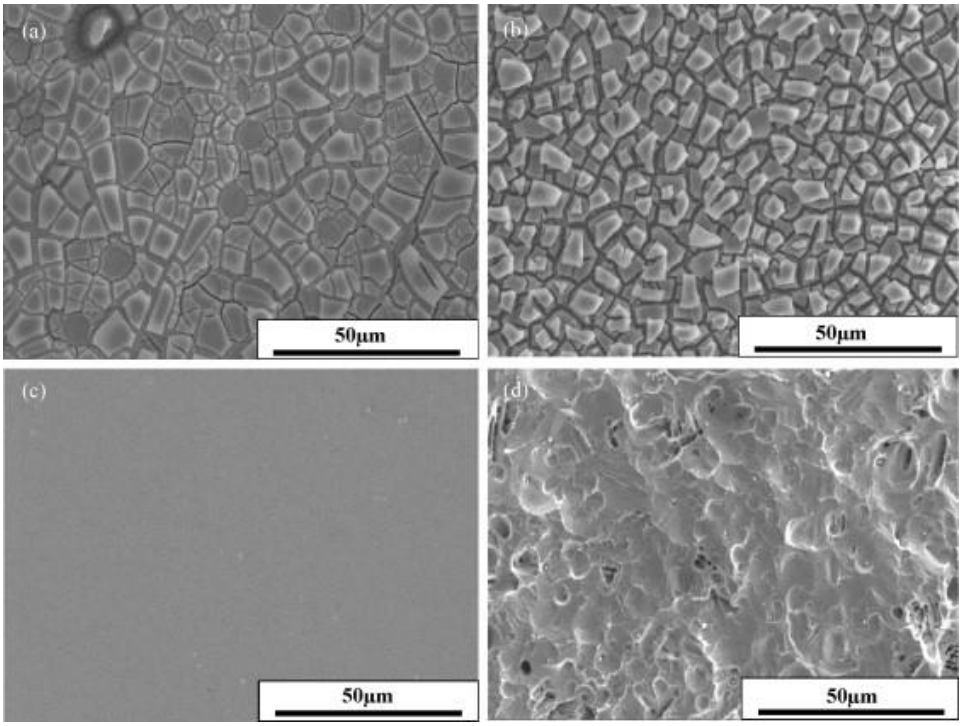

Fig. 17 Microstructures of corroded surfaces with (a) 0, (b) 2.3, (c) 12.3 % Cr, and (d) SUS304 alloy in 1N HCl solution [14]. (Image reprinted with permission from ELSEVIER).

prevents the dissolution of surface elements below the film, thereby offering high passivation potential. This is clearly visible in the SEM micrographs of the corroded surfaces presented in Fig. 17. In addition, surface homogeneity is believed to have contributed to the superior resistance. The absence of grain boundaries, twins, dislocations, and impurities lead to structural homogeneity, resulting in avoiding micro-cells and pitting and in turn contributing to the formation of a stable passive film [14].

Fe based metallic glasses are known to be extremely brittle resulting in sudden failure that can be catastrophic and thereby has limited structural applications despite superior wear resistance. Although these metallic glasses exhibit excellent wear resistance, their tribological performance at elevated temperatures has been relatively unexplored. Sliding wear behavior of $Fe_{66.7}C_{7.0}Si_{3.3}B_{5.5}P_{8.7}Cr_{2.3}Al_{2.0}Mo_{4.5}$ metallic glass was evaluated. The alloy exhibited a yield

strength of 3400 MPa under compression at room temperature. The chemical and mechanical interaction between the sliding pin and metallic glass, both contribute to the wear behavior of the metallic glass at high temperatures. It was observed that with an increase in temperature up to 810 K, the wear loss decreased up to 790 K and then increased further as the temperature went up. At all loads, wear loss at 790 K and 810 K was lowest than that recorded at other temperatures. This change can indicate a transition in wear behavior from brittle to fracture or oxidation mechanisms. The friction coefficient at lower temperatures recorded a high value in the beginning but stabilized later with sliding speed. As the temperature increased, the friction coefficient decreased due to high deformation rate of viscosity in the supercooled liquid region. The microscopic analysis of the wear track revealed abrasive wear in the metallic glass due to the high amount of oxygen in the tribo-layer acting as the media. Due to high temperature, the elements in the metallic glass alloy tend to form oxides that appear as bright particles on the surface. These particles in turn act as abrasive media resulting in grooves and plowing phenomenon on the surface of the metallic glass. In addition, plastic deformation on the worn surface was also indicated by the presence of grooves, tears, and voids on the metallic glass [45].

Fe based metallic glasses were developed as composites and composite coatings by reinforcing with hard crystalline phases. A mixture of $Fe_{68.8}C_7Si_{3.5}B_5P_{9.6}Cr_{2.1}Mo_2Al_2$ (at. %) metallic glass powder and the B_4C powder was spray coated on mild steel substrates using plasma spray. It was observed that the wear behavior of the coating greatly improved by embedding B_4C in the relatively soft matrix. The hardness of the composite increased which in turn contributed to the inhibition of plastic flow. This has resulted in low friction coefficients and low wear losses. B_4C acts as solid lubricant resulting in low two-body abrasive wear. The worn surface was characterized by the presence of grooves and cracks. As plasma sprayed coatings are very porous in nature, these pores may have caused formation and propagation of cracks. Although metallic glasses and metallic glass composite coating has shown signs of plastic deformation, in the

composite coating the deformation was limited to within the B_4C particle in the amorphous matrix. The worn surface displayed elongated and deformed metallic glass coating (as seen in Fig. 18 (a)), that is a characteristic of the superplastic of the metallic glass during wear. This plastic deformation may have also been caused due to increase in glass transition temperature to that of crystallization temperature during wear [15].

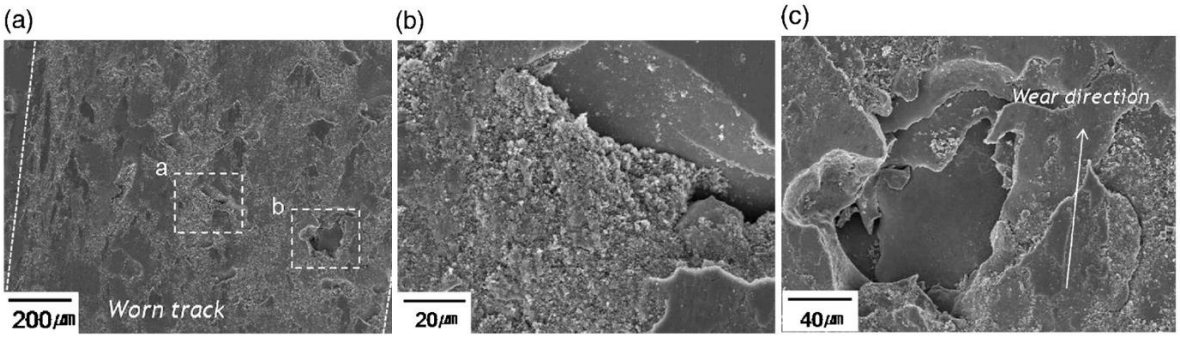

Fig. 18 SEM micrographs of **(**a) worn surfaces of amorphous alloy coating with 0 % B_4C, and (b, c) magnified images of areas marked in (a) [15]. (Image reprinted with permission from ELSEVIER).

1.3 Hypothesis and Objectives

1.3.1 Bulk metallic glasses as coatings

Cu-Ni alloys are one of the most widely used materials in the field of marine engineering [46, 47]. From ship hulls to seawater tankers, desalination plants, piping in hydraulic suspension systems, and offshore oil rigs, numerous applications can be found due to their excellent corrosion resistance and resistance to biofouling [48]. Although these alloys have good strength, surface deformation on the application of load limits their applications in mechanical components. To utilize Cu-Ni alloys in manufacturing mechanical components, it is important that their wear resistance is improved to avoid frequent refurbishments. While several surface engineering approaches are available to improve the wear resistance of metallic substrates, it is challenging to find processes and coating materials that improve wear resistance without sacrificing corrosion resistance for marine applications.

Amorphous alloys are known to exhibit higher strength, hardness, and wear and corrosion resistance when compared to their polycrystalline counterparts. This can be attributed to the defect-free disordered atomic structure found in amorphous materials [21].

However, certain undesirable characteristics such as high brittleness and low ductility make processing of these alloys into complex shapes a challenge. These characteristics have restricted the commercial use of amorphous alloys in structural applications. In lieu, development of these amorphous alloys as possible coating materials to make use of their high strength, wear and corrosion resistance was investigated. Zr–, Ni–, Cu–, and Fe– based amorphous alloys have been explored as coating materials based on desired corrosion resistant [49] and wear resistant properties [50]. In particular, Fe– based amorphous alloys exhibit good magnetic properties [51, 52], high strength and toughness [53, 54], high plasticity [55], corrosion and wear resistance [56, 57]. Over other amorphous alloys, Fe–based amorphous alloy with composition $Fe_{48}Cr_{15}Mo_{14}Y_2C_{15}B_6$ exhibits good glass forming ability along with excellent wear and corrosion

resistance [56, 58]. Also, this alloy has a low critical cooling rate which facilitates its deposition as coatings using thermal spray techniques [59]. Conventional coating techniques such as air plasma spray (APS) [60], high velocity oxy-fuel (HVOF) spray [56, 61, 62], kinetic spray [63], detonation gun spray [64], along with new approaches such as laser cladding [65], have been used to deposit these amorphous alloy coatings. Although these techniques were successful in retaining the amorphous phase of these coatings, they have been restricted due to limitations such as poor density, oxidation, partial devitrification, and poor interfacial strength between the coating and the substrate. Recently, spark plasma sintering (SPS) is increasingly being considered for the processing of thick coatings [66-68]. SPS involves the application of uniaxial pressure and passing pulsed direct current through the powder kept in graphite dies, and the sintering of powder occurs primarily due to Joule heating at the particle contacts [69, 70]. With possibilities of sintering at relatively lower temperatures and in shorter sintering times, SPS presents significant promise for the manufacturing of amorphous alloys and composites [71, 72]. It has also been reported that the activation energy of viscous flow during SPS of Fe-based amorphous alloys decreases with increasing heating rate [23, 25]. Since retention of the amorphous phase to the maximum extent possible is desirable, the above characteristics make SPS well suited for the processing of amorphous alloy coatings in niche applications [73, 74]. While powder metallurgy-based technologies have been extensively studied for the processing of coatings, the difficulty in scalability often limit the broader applications of this processing. The issues related to scalability of SPS technologies are well recognized, and significant progress has been made to scale up the processes using larger power supplies (up to 50,000 A) and pressing force (2,000 kN). These developments indicate the significant promise of SPS technologies in the manufacturing of thicker coatings of a range of materials, including amorphous alloys.

Objective I- Study of Spark plasma sintering of Fe-based metallic glass as coatings and evaluation of tribological characteristics.

In the present work, processing of Fe-based amorphous alloy ($Fe_{48}Cr_{15}Mo_{14}Y_2C_{15}B_6$) coatings on Cu–10%Ni alloy using SPS is reported. The coatings are processed at several sintering temperatures (575-675 °C), and the effect of SPS sintering temperature on the development of phases, microstructure, hardness, and wear characteristics of the coatings is investigated.

1.3.2 Bulk metallic glass composites

Bulk metallic glasses, including Fe-based compositions, are known for their high strength and superior resistance to wear and corrosion when compared to their polycrystalline counterparts [75, 76]. However, the actual utilization of metallic glasses in structural applications is restricted primarily due to difficulty in scalable manufacturing and low ductility of the alloys.

Among several approaches developed, spark plasma sintering (SPS) presents a significant potential for scalable manufacturing of ex-situ bulk metallic glass composites with high general ductility [74]. For example, Kim et al. reported substantial improvement in compressive plastic strain for SPS sintered Cu-based metallic glass composites reinforced with 20-40 vol.% Cu particles [77]. While, the improvement in ductility for the SPS sintered ex-situ composites is well demonstrated, the wear and corrosion properties of these composites are not well investigated. Kwon et al. reported on wear behavior of SPS sintered Fe-based metallic glass composites reinforced with 5-50 vol.% Ni [78]. In this study, Ni was deposited on the metallic glass powder using electroless plating prior to sintering, and the volume fraction was controlled by the thickness of the coatings. It was observed that the wear resistance of the composites improves with reinforcement of 5 and 10 vol.% Ni due to higher toughness of these composites compared to monolithic metallic glass. However, the composites reinforced with higher amounts (20-50

vol.%) of Ni displayed excessive damage due to accelerated adhesive wear [78].

However, systematic evaluation of SPS sintered ex-situ metallic glass composites, especially at lower reinforcement contents (<10 vol.%), for both wear and corrosion behavior has not been reported. In this study, we investigated the corrosion and wear behavior of SPS sintered Fe-based bulk metallic glass ($Fe_{48}Cr_{15}Mo_{14}Y_2C_{15}B_6$) composites reinforced with up to 10 vol.% Ni. Instead of electroless plating as reported in the previous publication, Ni reinforcement was accomplished by mixing the constituent powders prior to SPS sintering.

Objective II- Study of spark plasma sintered Fe-based metallic glass composites and evaluation of its electrochemical and tribological behavior.

In this study, we investigated the corrosion and wear behavior of SPS sintered Fe-based bulk metallic glass ($Fe_{48}Cr_{15}Mo_{14}Y_2C_{15}B_6$) composites reinforced with up to 10 vol.% Ni. Instead of electroless plating as reported in the previous publication, Ni reinforcement was accomplished by mixing the constituent powders prior to SPS sintering.

.

CHAPTER II

MATERIALS AND METHODS

2.1 Spark plasmas sintering of $Fe_{48}Cr_{15}Mo_{14}Y_2C_{15}B_6$ coatings on Cu-10% Ni alloy.

Fe–based amorphous alloy powder with overall composition $Fe_{48}Cr_{15}Mo_{14}Y_2C_{15}B_6$ (at.%) was used to fabricate coatings using SPS on Cu–10%Ni alloy substrates. The amorphous powder exhibited a normal distribution of particle sizes with about 90% of the particles in the size range of 20-60 μm and a mean size of 40 μm. Differential scanning calorimetry (DSC) analysis of this amorphous alloy powder revealed the glass transition temperature of 575 ˚C and the crystallization temperature of 653 ˚C [33, 34]. The Cu-Ni alloy substrates used were 15 mm in diameter and 4 mm in thickness. The substrates were thoroughly polished using 240, 400, and 600 grit abrasive papers. A commercial SPS machine (Thermal Technology Inc., Santa Rosa, USA) was used to sinter the coatings. Each polished substrate was degreased using alcohol and acetone and placed inside a graphite die. About 0.6 g of the powder was placed on the substrate and sintered with a uniaxial pressure of 50 MPa, a heating rate of 100 ˚Cmin-1, and holding time of 10 min at different sintering temperatures (575, 600, 625, 650 and 675 ˚C). After sintering, the samples were prepared using metallographic techniques to facilitate characterization for microstructure. A scanning electron microscope (JEOL Ltd, Tokyo, Japan) was used to study the prepared cross-sections of the coatings.

The average thickness of these coatings was in the range of 300 – 460 µm. Phase analysis was carried out using a Philips Norelco x-ray diffractometer (XRD) operating with Cu–Kα radiation (λ = 1.54178 Å). A Vickers micro-hardness tester (Clark Instruments, Michigan, USA) was used to measure the hardness with a load of 100 g and dwell time of 15 sec. Sliding wear tests were performed using a ball-on-disc tribometer (Nanovea, Irvine, CA) with an alumina (Al2O3) ball of 6 mm diameter as the counter body sliding against sintered coatings (load of 20 N and sliding velocity of 200 rpm). Each wear test was run for a total duration of 50 min., and weight loss and coefficient of friction was recorded. The worn surfaces were observed under SEM to analyze wear mechanisms.

2.2 Spark plasma sintering of Ni-reinforced $Fe_{48}Cr_{15}Mo_{14}Y_2C_{15}B_6$ metallic glass composites

Fe-based bulk metallic glass powder of composition $Fe_{48}Cr_{15}Mo_{14}Y_2C_{15}B_6$ (at. %) and average particle size of 45 µm was mixed with Ni powder (Alfa Aesar, USA) of particle size about 2-10 µm in a ball mill. The composite powders of five compositions (0, 2.5, 5.0, 7.5, and 10 vol.% Ni) were prepared. A commercial SPS system (Thermal Technology LLC, USA) was used to sinter the composites at 600 ˚C with applied pressure of 50 MPa, heating rate of 50 ˚C/min, and holding time of 10 min. A scanning electron microscope equipped with an EDS detector (FEI Company, USA) was used for microstructural and compositional analysis. Phase analysis was performed using an x-ray diffractometer (Philips, USA) operating with Cu–K_α radiation. Hardness of the composites was measured using a Vickers micro-hardness tester (Clark Instruments, USA) with a load of 100 g. Dry sliding wear tests were performed on the composite samples using a 6-mm diameter Al_2O_3 ball with a load of 20 N and sliding velocity of 200 rpm (Nanovea, USA). Potentiodynamic corrosion tests on the composites were performed using a three-electrode cell (platinum counter electrode and Ag/AgCl reference electrode) in 1 N HCl solution with a potential sweep rate of 0.167 mV/s.

CHAPTER III

RESULTS

3.1. Spark plasma sintering of $Fe_{48}Cr_{15}Mo_{14}Y_2C_{15}B_6$ metallic glass coatings on Cu-Ni alloy.

3.1.1 Microstructure

Fig. 19 presents the cross-sectional micrographs of the amorphous alloy coatings fabricated on Cu-Ni substrates at SPS temperatures 575, 600, 625, 650, and 675 ˚C. The coatings deposited at all the temperatures were near fully dense with minor porosity mostly near the surface of the coatings. It can be observed that the coatings exhibited good bonding with the underlying substrates. Some distributed porosity was observed for the coatings sintered at lower temperatures up to 625 ˚C (Fig. 1(b-d)). The interface was not very discernible in the coatings sintered at higher temperatures (650 and 675 ˚C), as shown in Fig. 1(e-f). The glass transition and crystallization temperature of the Fe-based amorphous alloy used in this investigation are 575 and 653 ˚C, respectively [79]. It is well known that amorphous alloys undergo significant superplastic-like deformation between the glass transition and crystallization temperatures (supercooled liquid range). All the above-mentioned coatings investigated in this study were either sintered in the supercooled liquid region or pass through this temperature range. As fully dense coatings were observed at the lowest sintering temperature of 575 ˚C in the supercooled liquid region, there is no further driving force for densification with increasing sintering temperatures.

.

The increasing sintering temperature, however, appeared to improve the interface characteristics of the coatings. The elemental distribution across the coating-substrate interface is shown in Fig. 20 and the elemental map is presented in Fig. 21. The EDS analysis designates the presence of primary elements in Cu-Ni substrate and amorphous alloy coating. It can also be observed from the elemental distribution that the interface is very distinct, and the change in composition from coating to substrate occurs over a very small distance (~2 μm). In the case of sintering of amorphous alloy coating on Cu-Ni substrate, the inter-diffusion is very limited.

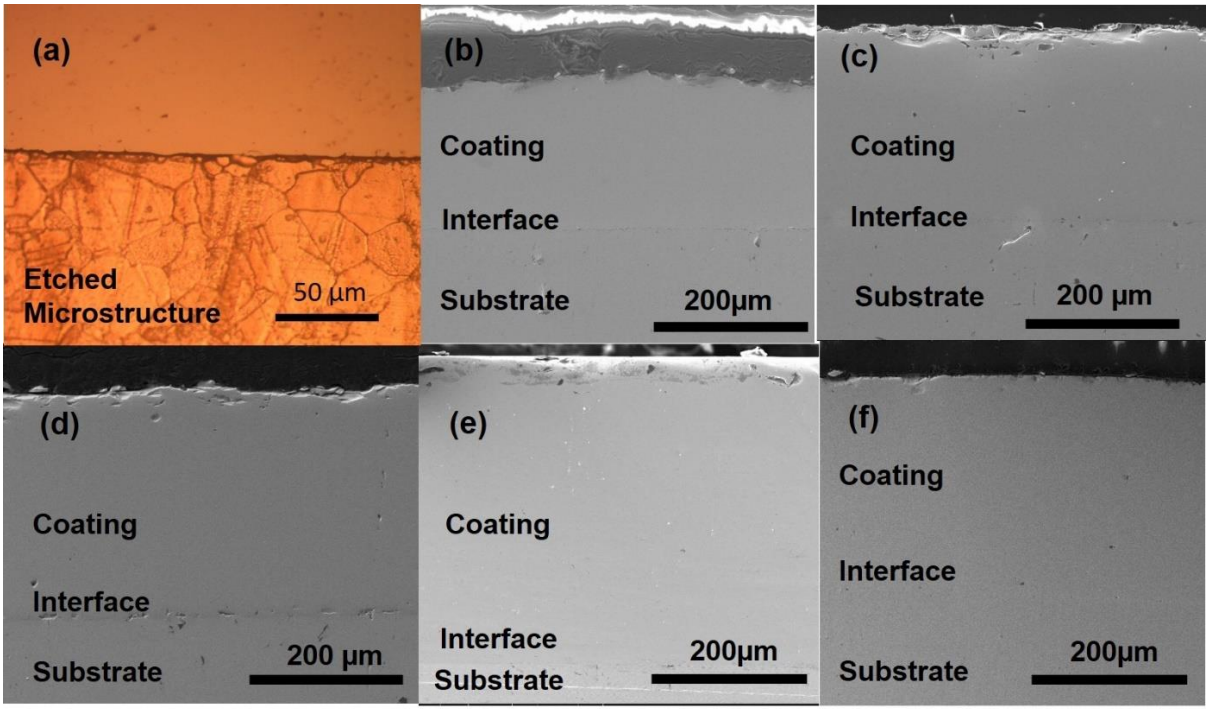

Fig. 19 SEM micrographs displaying (a) representative image of etched surface and interface of the coating; and coatings sintered at (b) 575, (c) 600, (d) 625, (e) 650, and (f) 675 ˚C.

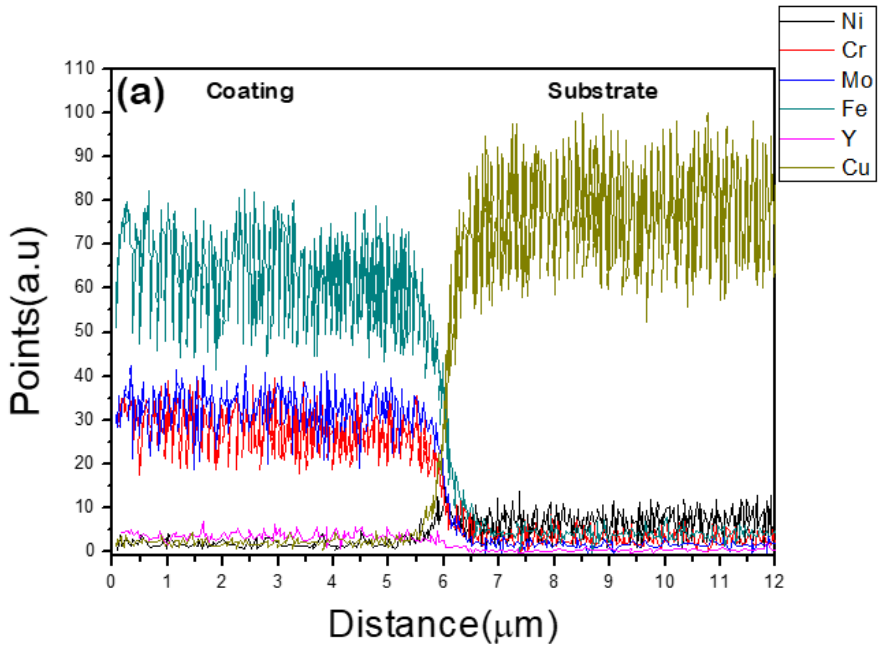

Fig. 20 EDS line scan across the interface.

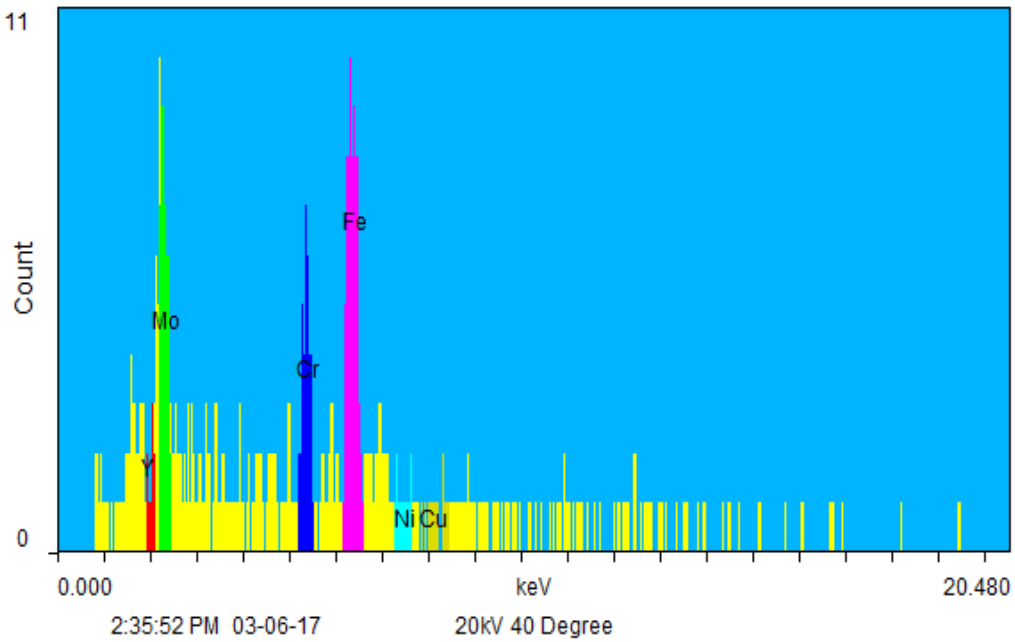

Fig. 21 Elemental distribution across the interface.

During the process of sintering amorphous coatings, the substrate discs were also heated up to sintering temperatures. The interfacial effects were mostly determined by the thermophysical properties of the substrate and coatings. For low melting substrates such as aluminum alloys, it has been observed that substrate material infiltrates into the overlaid amorphous powder across the full thickness (~400 μm) of the amorphous coatings at the sintering temperatures of 560-590 ˚C [68]. In case of Cu-Ni substrates with a melting point of about 1100-1150 ˚C, no such infiltration was observed for the sintering temperatures of 575-675 ˚C. It can be inferred that; the selection of sintering temperature must be made based on the possibility of retaining the fully amorphous structure of the coatings while minimizing the possibilities of material infiltration in the coating. The SPS can thus be used to sinter Fe-based amorphous coatings on substrates with a melting point about twice the sintering temperature in the supercooled temperature region of the amorphous alloy.

3.1.2 Phase Analysis

XRD pattern of the raw amorphous alloy powder is presented in Fig. 22. The pattern shows a broad diffused peak centered at a diffraction angle (2θ) of about 42.5°, confirming the amorphous structure of the powder. The starting amorphous powder was used to sinter the coatings on the Cu-Ni substrates to improve the possibility of retaining the amorphous structure in the coatings. Fig. 23 presents XRD patterns of amorphous coatings sintered at different sintering temperatures. All the coatings exhibited major diffused peak with superimposed crystalline peaks. Please note that crystalline phases are highly diffracting compared to the amorphous structure, and hence, the coatings are still predominantly amorphous, even with the presence of sharper crystalline peaks in the XRD patterns. This is consistent with the featureless microstructures observed for the sintered coatings indicating a predominantly amorphous structure. The sharper crystalline peaks were observed to be from $(Fe, Cr)_{23}(C, B)_6$ and $(Fe, Cr)_7(C, B)_3$ phases. With increasing sintering temperature, the intensity of the primary crystalline peak at 2θ=44 ° shows a general increase in

intensity with increasing SPS sintering temperature. Also, new peaks appear in the XRD patterns for coatings sintering at a higher temperature, indicating increasing devitrification of amorphous coatings with increasing sintering temperature.

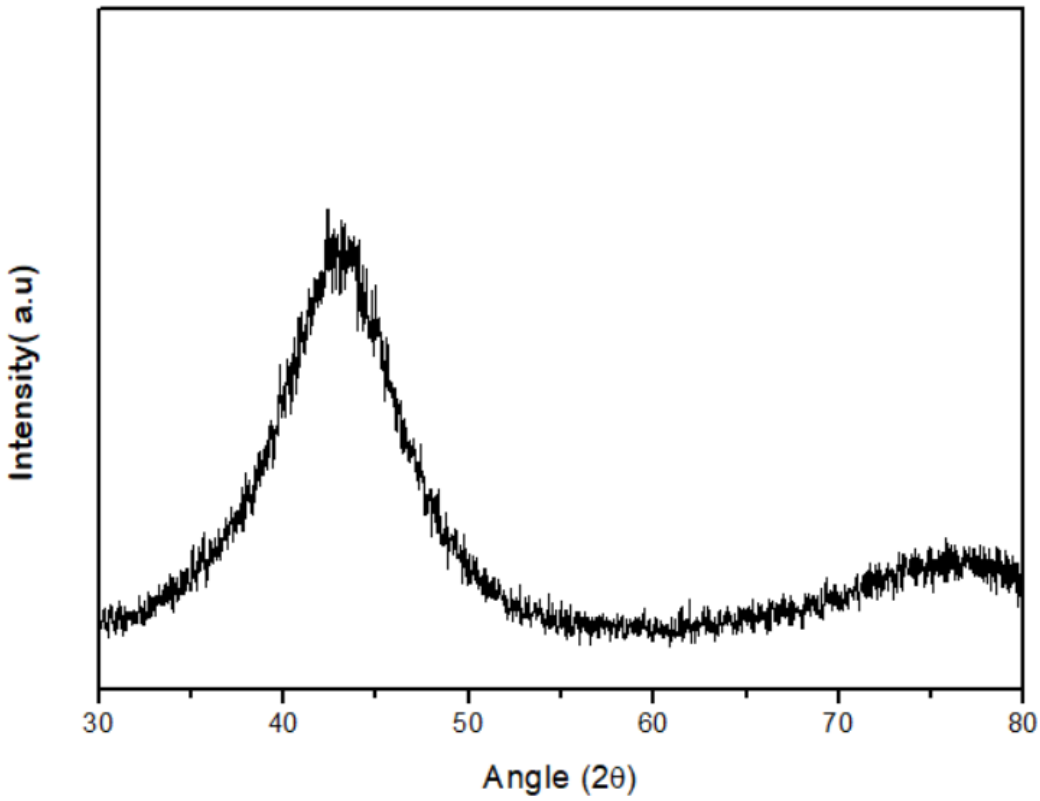

Fig. 22 XRD pattern of pure Fe based metallic glass powders used to sinter coatings.

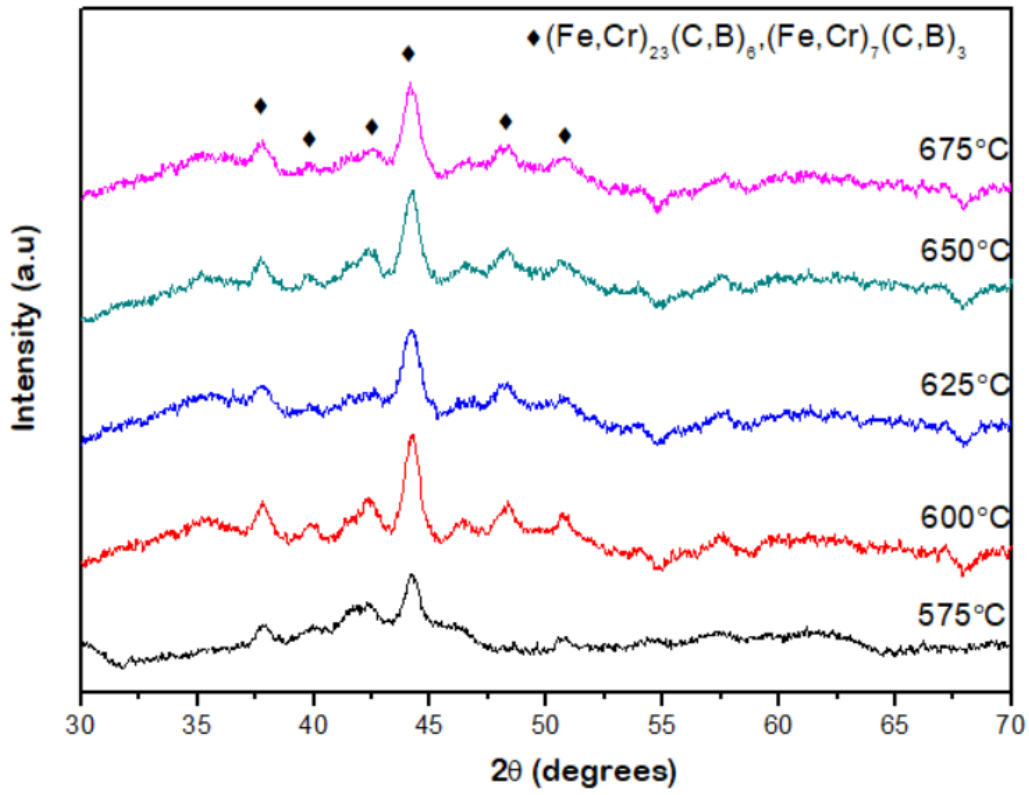

Fig. 23 XRD patterns of coatings sintered at temperatures ranging from 575 to 675 ˚C.

The reported crystallization temperature of the Fe-based amorphous alloy used in this investigation is 653 ˚C. The sintering temperature was measured using a thermocouple placed in the die wall (about 2 mm from the internal surface). The temperature at the center of the sample is possibly higher than that recorded by the thermocouple. It is well reported that the temperature at the center of the die could be as much as 30 ˚C higher than the temperature at the edge of the sample [80]. The extent of this overheating depends on the heating rate and is also likely to be higher for the sintering of powder coatings on monolithic substrates. It should also be noted that SPS sintering even in the supercooled liquid region is reported to result in local structural/compositional changes associated with nucleation of nano-scale clusters [79]. The

appearance of crystalline peaks in the amorphous coatings sintered in the supercooled liquid region is likely due to these localized effects.

3.1.3 Hardness

The microhardness profiles along the depth of the amorphous alloy coatings sintered at various temperatures are presented in Fig. 24. The average surface micro-hardness values of the coatings SPS sintered at 575, 600, 625, 650, and 675 ˚C was 1242, 1168, 1232, 1319, and 1202 HV, respectively and is tabulated in Table. 1. The hardness of the Cu-Ni substrate was about 90-110 HV. While a clear trend in the variation of surface microhardness of the coatings with increasing sintering temperature was not established, the hardness remained relatively uniform up to the depth of about 200-250 μm in the coatings followed by a continuous decrease to the hardness of the substrate. The observed hardness of the sintered amorphous alloy coatings (~1200-1400 HV) was close to the hardness of SPS sintered dense monolithic amorphous alloy of similar compositions [81]. For example, the hardness of Fe-based amorphous alloy of composition $Fe_{49.7}Cr_{17.1}Mn_{1.9}Mo_{7.4}W_{1.6}B_{15.2}C_{3.8}Si_{2.4}$ processed through SPS is reported to be in the range of 1150-1250 HV. [71]Various other coating techniques such as air plasma spray [82], high-velocity oxygen fuel [58], and detonation gun [64] have been used to process Fe-based amorphous coatings. The porosity of these detonation gun sprayed coatings when evaluated using image analysis is reported to be ~ 2% [64]. Also, the hardness of Fe-based amorphous coatings generated using air plasma spray, high-velocity oxygen fuel, and wire arc spraying was found to be in the range of 900 – 1100 HV [62, 83]. On the other hand, coatings sintered using SPS showed negligible porosity. SPS appears to be well suited for the fabrication of dense thick coatings of amorphous alloys. A comparison of various coatings techniques and hardness values of coatings generated from these techniques is presented in Table 2.

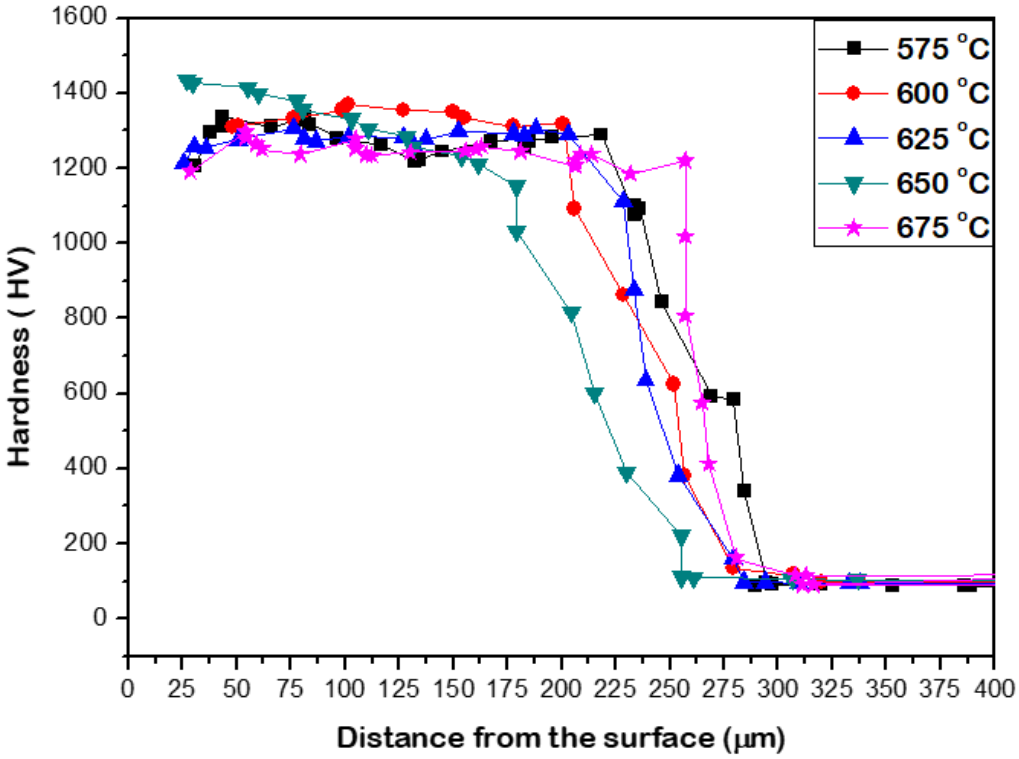

Fig. 24 Variation in microhardness of the coatings sintered at different temperatures from the surface to the substrate.

Table 1 Variation in micro-hardness values with temperature.

Temperature (˚C)	**Hardness ($HV_{0.1}$)**
575	1242 ± 150
600	1168 ± 50
625	1232 ± 58
650	1319 ± 135
675	1202 ± 105

Table 2 Comparison of the hardness of coatings generated using various thermal spray technologies with spark plasma sintering.

Process	Coating Composition (at. %)	Substrate	Hardness (HV)
Air Plasma Spray	$Fe_{40.15}Cr_{18.03}Mo_{21.91}C_{18.25}Si_{1.66}$	Mild Steel	1100
High-Velocity Oxygen Fuel Spraying	$Fe_{52.2}Cr_{18.9}B_{16.1}C_{4.0}Si_{2.8}Mo_{2.4}Mn_{1.9}W_{1.7}$	Mild Steel	930
Wire arc spraying process	$Fe_{64.82}B_{20.69}Si_{1.9}Cr_{9.23}Nb_{1.8}Mn_{1.01}Y_{0.55}$	Stainless Steel	900-1050
Spark Plasma Sintering	$Fe_{48}Cr_{15}Mo_{14}C_{15}B_6Y_2$	Cu-Ni	1200-1400

3.1.4 Tribological Analysis

The variations of volume wear rate and coefficient of friction (COF) of the SPS sintered amorphous coatings with sintering temperature are presented in Fig. 25. It can be observed that the wear rate showed a general decreasing trend while the COF slightly increased with increasing sintering temperature from 575 to 650 ˚C. It is well established that although amorphous alloys exhibit high hardness, they are brittle in nature. For the coatings sintered at 575 ˚C, although partial devitrification was observed, the presence of broad halo indicated the presence of dominant amorphous phase. The high wear rate of the coatings sintered at 575 ˚C can, therefore, be explained by the brittle nature of the dominant amorphous phase. Further increase in sintering temperature causes increased devitrification of the coatings as observed from the XRD profiles. It has been well established that as nanocrystalline phases formed in the amorphous matrix due to thermal devitrification causes hardening and the associated increase in wear resistance [84]. In

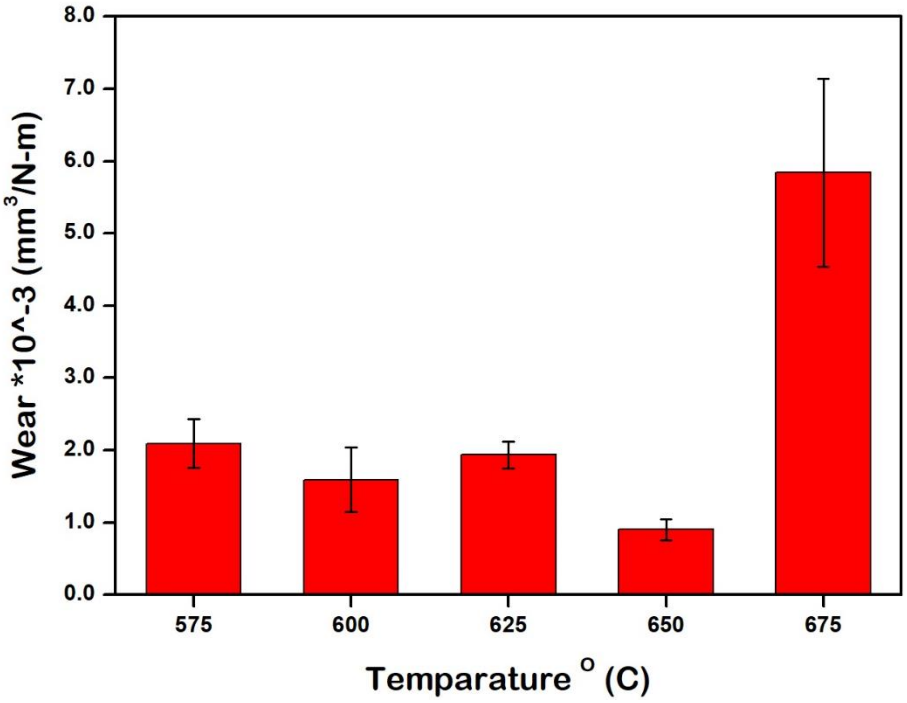

Fig. 25 Variation in wear rate of coatings with sintering temperature.

fact, the coatings sintered at 650 ˚C exhibited highest surface hardness and lowest wear rate among the sintered samples.

However, when the sintering temperature was increased from 650 to 675 ˚C, a significant increase in wear rate was observed. It appeared that embrittlement due to excessive devitrification of the amorphous alloy at this highest sintering temperature resulted in severe wear of the coatings. Figs. 26 presents the variation of the friction coefficient (COF) with temperature. It can be seen that the variation in COF is negligible. Fig. 27 present the low and high magnification images of the wear surfaces of the sintered amorphous coatings. The coatings sintered at 575 ˚C exhibited deep scratches and grooves along the sliding direction indicative of abrasive wear mechanism (Fig. 28(a)).

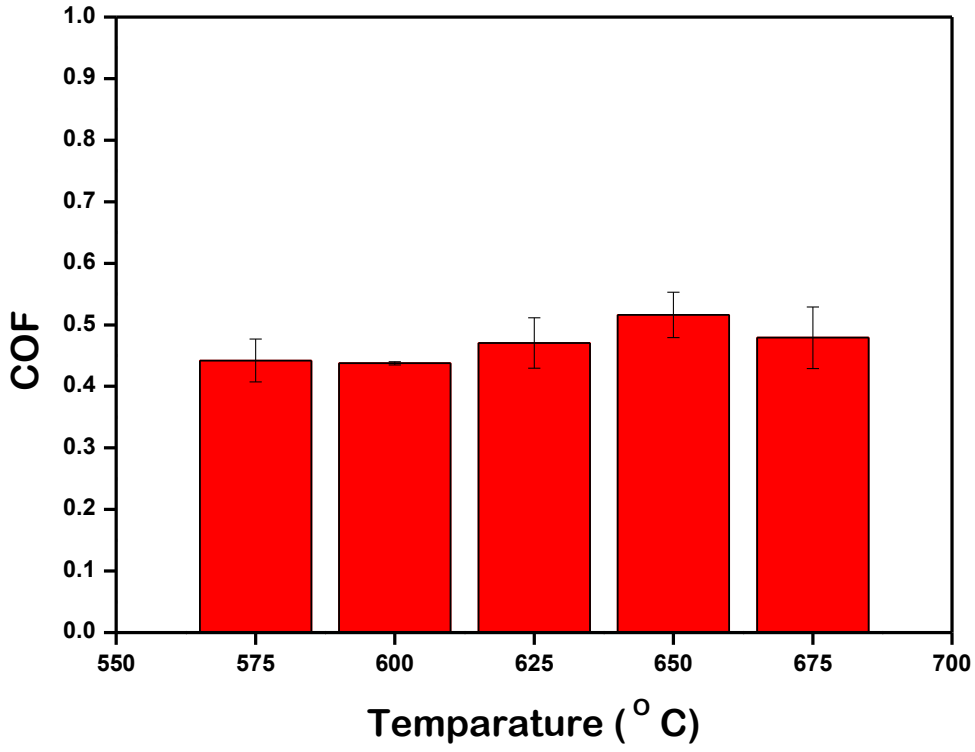

Fig. 26 Variation in the friction coefficient of the coatings with sintering temperature.

These coatings also showed some cracking and chipping most likely initiated at the sites of porosity in the sintered coatings. The coatings sintered at higher temperatures showed the formation of a scaly layer on the wear surface. The surface layer was relatively continuous but cracked for the coatings sintered at higher temperatures (Fig. 28(b)). It is well known that the Fe-based amorphous alloys undergo surface oxidation under dry sliding wear conditions [84]. As the coatings sintered at higher temperatures showed a higher degree of devitrification, it appears that devitrified coatings are more susceptible to the surface oxidation during sliding wear. The lower wear rate for the coatings sintered at 650 ˚C is likely due to surface hardening and formation of surface layer both linked to the higher degree of devitrification in these coatings. On the other hand, the coatings sintered at 675 ˚C showed extensive delamination of the scaly surface layer, which contributed to higher wear rate for these coatings (Fig. 28(c)). The wear results indicate

that the partial devitrification of the amorphous coatings improves the wear resistance by introducing surface hardening and formation of the protective surface layer for coatings sintered in the range of 575-650 ˚C. However, extensive devitrification observed for coatings sintered at a higher temperature (675 ˚C) causes embrittlement and break down of the protective layer, resulting in higher wear rate. Furthermore, the wear tests performed at high normal load in this investigation did not cause any delamination or fracture of the coating at the interface, indicating strong bonding between the SPS sintered amorphous coating and the substrate. However, further characterization of the mechanical properties and bond strength is necessary to assess the applicability of the proposed approach for the processing of thick amorphous coatings.

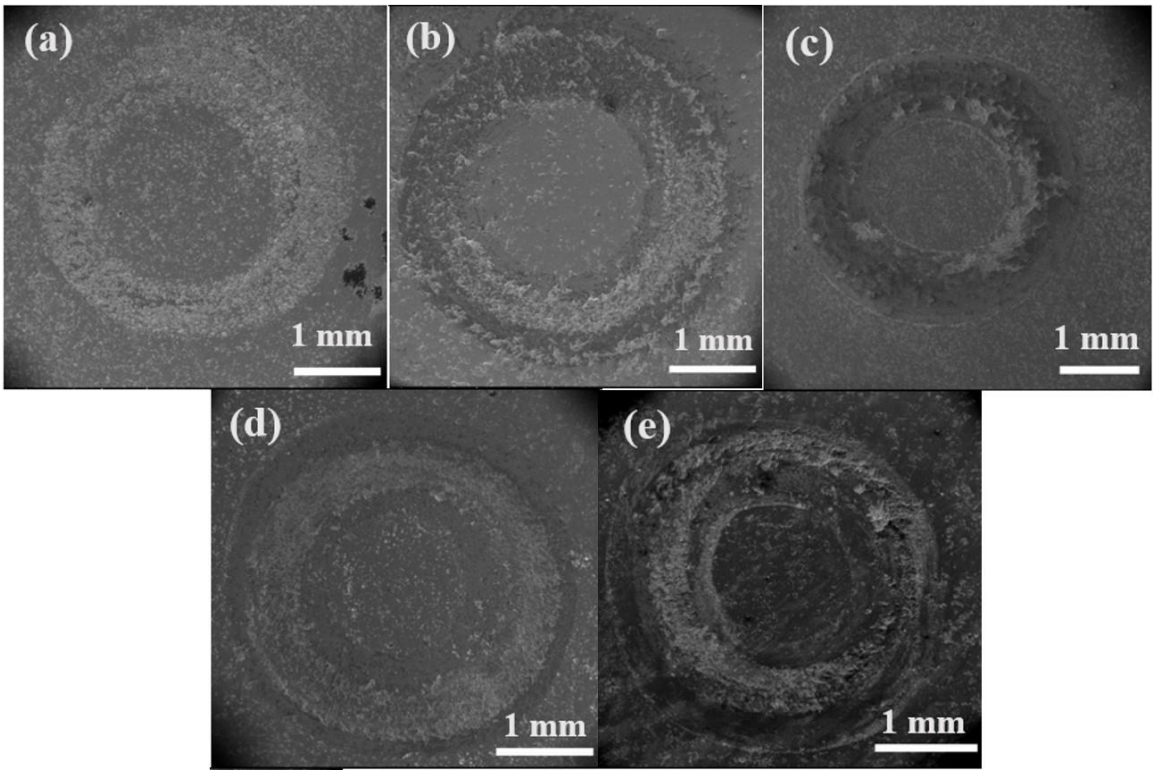

Fig. 27 SEM micrographs of worn surfaces of coatings sintered at (a) 575, (b) 600, (c) 625, (d) 650, and (e) 675 ˚C**.**

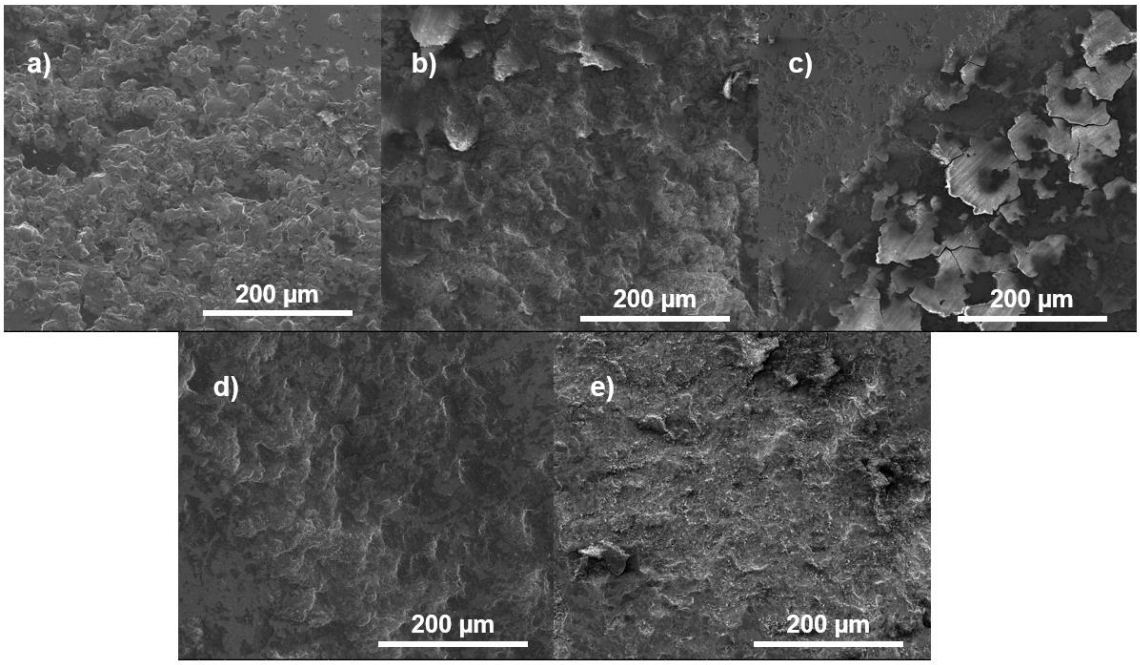

Fig. 28 High magnification SEM micrographs of features of worn surfaces for coatings sintered at (a) 575, (b)600, (c) 625, (d) 650, and (e) 675 ˚C.

3.2 Spark plasma sintering of Ni reinforced $Fe_{48}Cr_{15}Mo_{14}Y_2C_{15}B_6$ metallic glass composites.

3.2.1 Reinforcement of metallic glasses with ductile phase using ball milling

3.2.1.1 Microstructure and Phase analysis

The SEM micrographs and EDS spectrum of SPS sintered Ni reinforced Fe-based metallic glass composites (2.5 – 5 vol.% Ni) are presented in Fig. 29 and Fig. 30. The sintered composite samples were near fully dense with Ni distributed between the larger metallic glass particles (Fig. 29 (a)); the primary elements of the composites were also detected in EDS spectrum (Fig. 30). The XRD pattern from the un-reinforced metallic glass specimen showed a broad halo peak, indicating that amorphous structure was retained with the SPS processing parameters used (Fig. 31). As shown in the Fig. 32, the XRD patterns from the composites exhibited broad halo peaks indicative of the amorphous structure along with superimposed primary peaks from the Ni reinforcement [(111) and (200) peaks at about 44 and 52°, respectively]. The intensity of the Ni

peaks increased with increasing Ni content in the composites. In addition, the XRD patterns from the composites showed some minor peaks, possibly from the intermetallic phases formed due to reactions between Ni and constituents of metallic glass at the SPS sintering temperature.

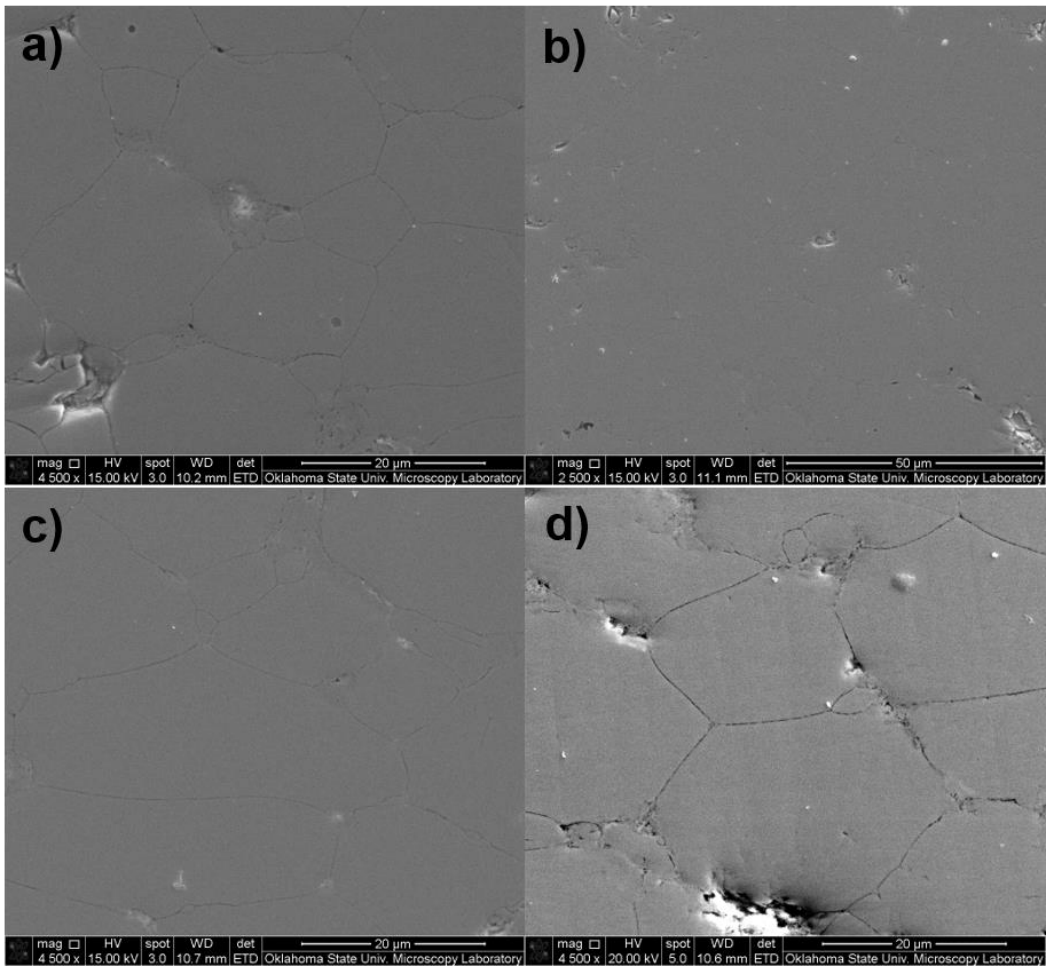

Fig. 29 SEM micrographs of surface of sintered composites with (a) 2.5, (b) 5, (c) 7.5, and (d) 10 % Nickel.

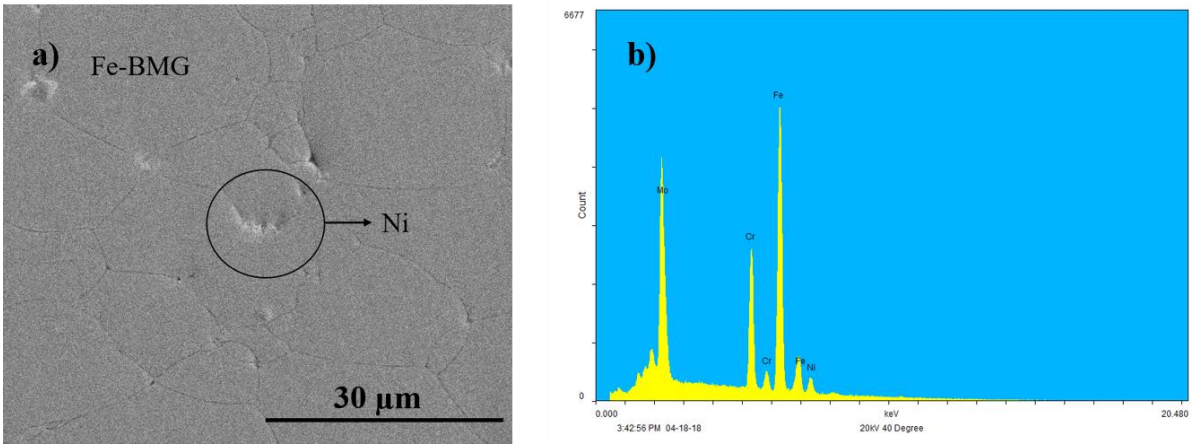

Fig. 30 (a) High magnification SEM image exhibiting dense composites, and (b) EDS analysis at a spot as indicated in (a).

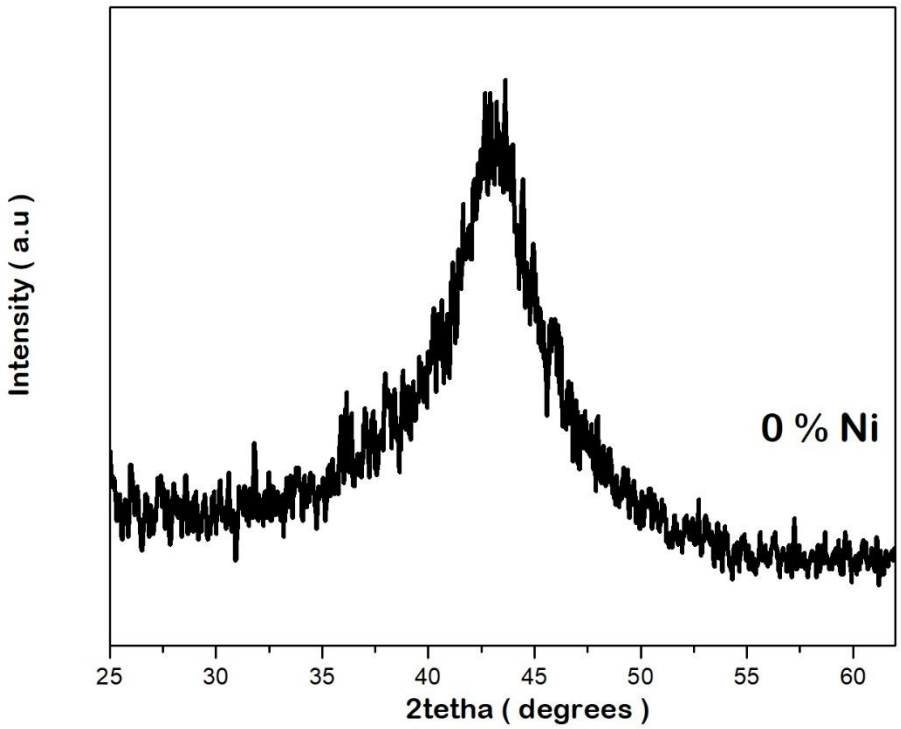

Fig. 31 XRD pattern of monolithic amorphous alloy disc sintered at 600 ˚C.

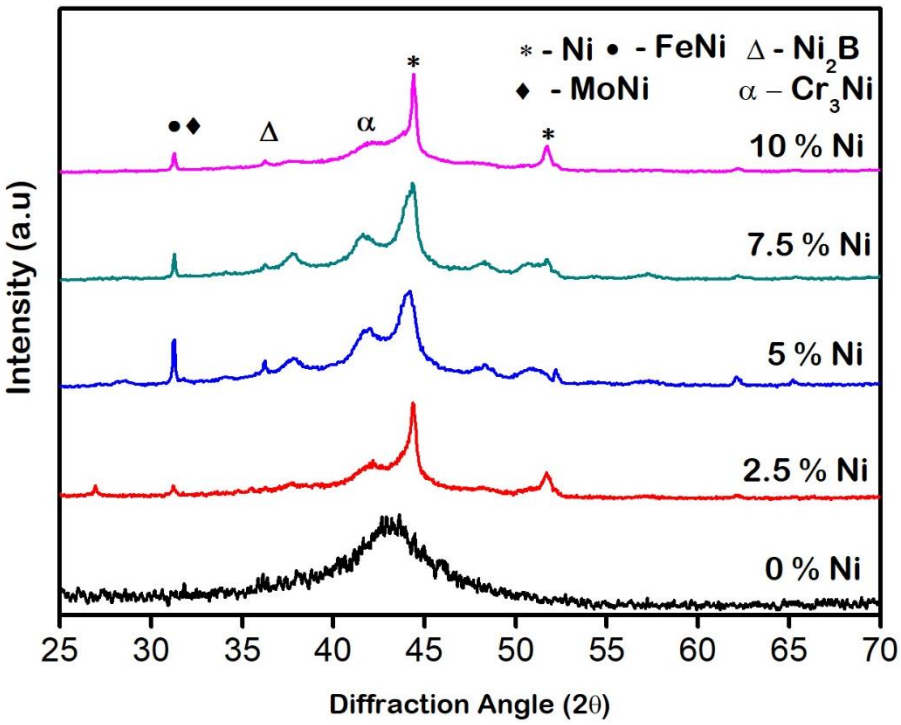

Fig. 32 XRD patterns of composites with varying nickel content.

3.2.1.2 Hardness

The microhardness of the sintered un-reinforced Fe-based metallic glass was observed to be in the range of 1200-1400 HV (Fig. 33), consistent with previous reports [85]. As Ni is a relatively softer phase with a hardness of about 120 HV, the hardness of the metallic glass composites continuously decreased with increasing Ni reinforcement content from 2.5 to 10 vol.%. The microhardness of composites reinforced with 2.5 and 10 vol.% Ni was about 1150 and 890 HV, respectively.

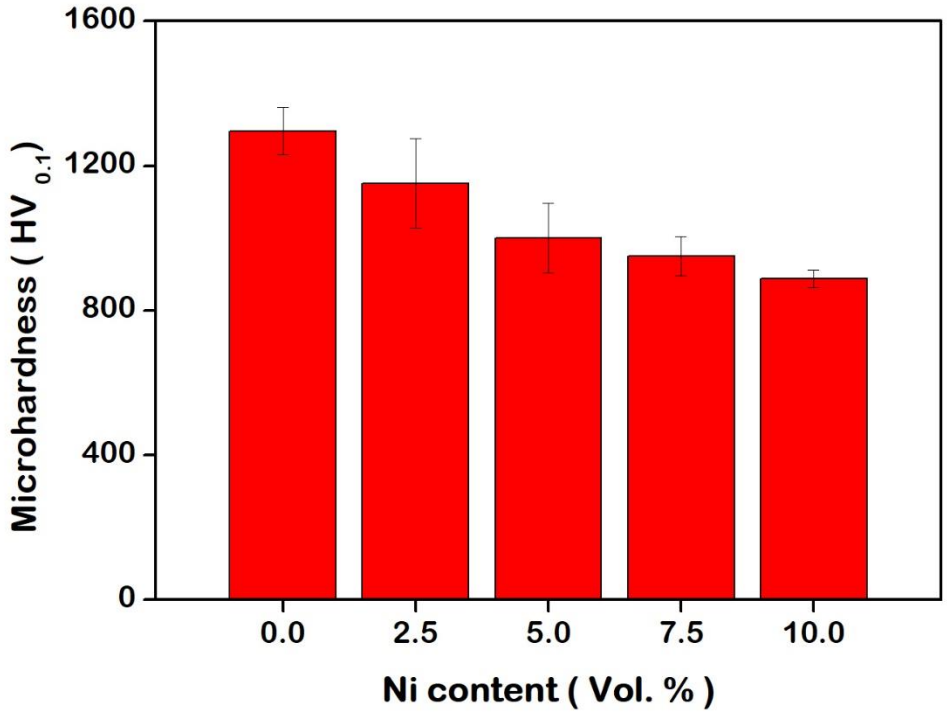

Fig. 433 Variation in microhardness of the composites with nickel content.

3.2.1.3 Corrosion behavior

The results from potentiodynamic polarization tests in 1N HCl solution are presented in Fig. 1(d). The sintered Fe-based metallic glass specimen displayed a smooth polarization curve with corrosion potential (E_{corr}) of -0.22 V and corrosion current density (I_{corr}) of 0.21×10^{-6} A/cm^2. The low I_{corr} can be attributed to the homogenous disordered structure of the metallic glass and is in good agreement with previous reports on as-cast $Fe_{48}Cr_{15}Mo_{14}Y_2C_{15}B_6$ metallic glass tested in HCl solution [86]. On the other hand, the corrosion resistance deteriorated with the reinforcement of Ni in metallic glass composites as indicated by a decrease in corrosion potential and increase in corrosion current density. Clearly, the presence of Ni and other reaction products in the sintered composites create local galvanic cells and also introduce interfaces, accelerating localized corrosion. While no clear trend was observed in term of the effect of reinforcement content on the

corrosion potential and current density of the composites, the specimens with lower reinforcement content (2.5 and 5 vol.% Ni) appear to exhibit some degree of passivation between -0.40 and -0.25 V before entering into the transpassive region.

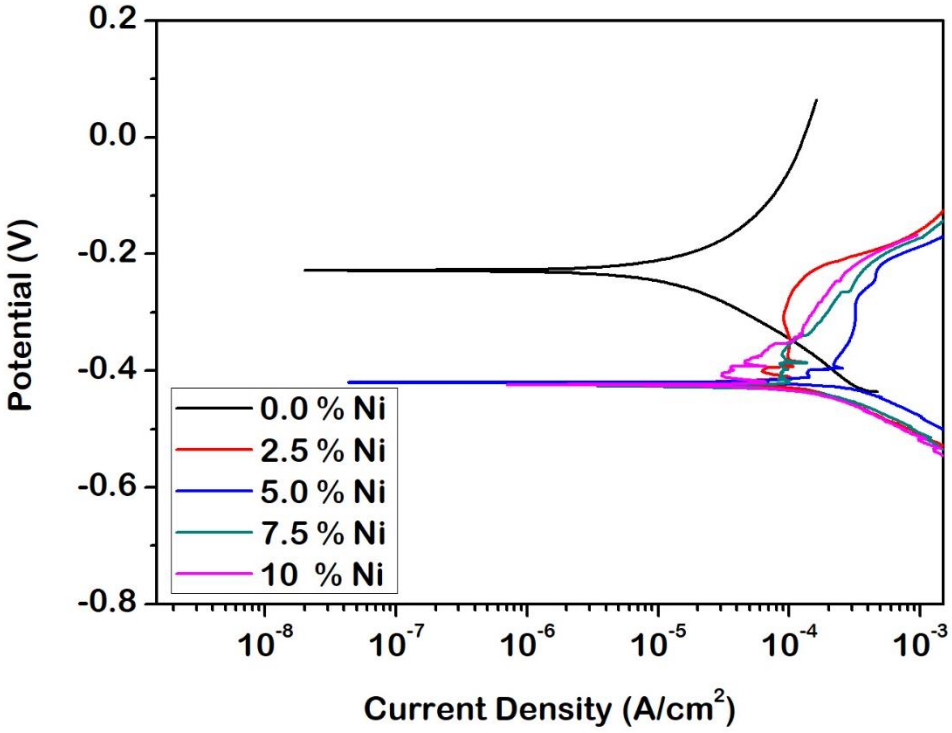

Fig. 34 Potentiodynamic polarization curves of composites with varying nickel content in 1N HCl solution.

The samples S2.5 and S5 exhibited a stable passive zone from -0.42V to -0.23V and -0.39V to -0.27 V respectively before developing into a trans passive region, S7.5 and S10 samples demonstrated a gradual evolution into the trans-passive region, without indicating the presence of a distinct passive region. Moreover, all samples exhibited a stable trans-passive region after 4.5×10^{-6} A/cm^2 with similar slopes (of Tafel plots) as seen in Fig. 34.

3.2.1.4 Tribology

The wear rates of SPS sintered monolithic metallic glass and its Ni reinforced composites are presented in Fig. 35. As the hardness of the composites decreased continuously with increasing Ni content, it was expected that the wear rate would follow the similar trend in accordance with the Archard's wear law. However, the composites reinforced with 2.5 and 5 vol.% Ni exhibited lower sliding wear rate even though these composites have lower hardness compared to monolithic metallic glass. At higher Ni reinforcement content (7.5 and 10 vol.%), the wear rate of composites is significantly higher than that for monolithic metallic glass. To investigate the wear mechanisms, examination of the wear surfaces was performed (Fig. 36). The wear surfaces of monolithic metallic glass showed deep grooves in the sliding direction indicative of abrasive wear behavior. It is also well recognized that dry sliding wear of Fe-based metallic glass causes surface oxidation, observed here as well by the presence of dark patches on the wear surface. The wear surface also shows microcracking, especially along the edges of these oxidation patches. As Fe-based metallic glass has a very low fracture toughness (3-4 MPa√m)[87], continued sliding causes brittle fracture of larger flakes of material from the wear track. The metallic glass composites with lower reinforcement content (2.5 and 5 vol.% Ni) exhibited relatively smoother worn surface covered with very fine surface debris (Fig. 36(b)), indicative of uniform material removal. The higher wear resistance of the composites at these reinforcement levels appears to be the direct consequence of expected improvement in fracture toughness due to softer/tougher Ni reinforcement; the fracture toughness of Ni is reported to be in the range of 80 to110 MPa√m. At higher reinforcement contents (7.5 and 10 vol.% Ni), the composites showed a relatively smoother surface with distributed regions (darker patches) of localized severe material removal (Fig. 36 (c)), indicating severe adhesive wear as reflected in high wear rates for these composites [78]. Clearly, the wear mechanism transitions from predominantly abrasive to adhesive with

increasing Ni content, with composites reinforced with intermediate Ni content (5 vol.%) showing optimum wear resistance among the compositions investigated in this study.

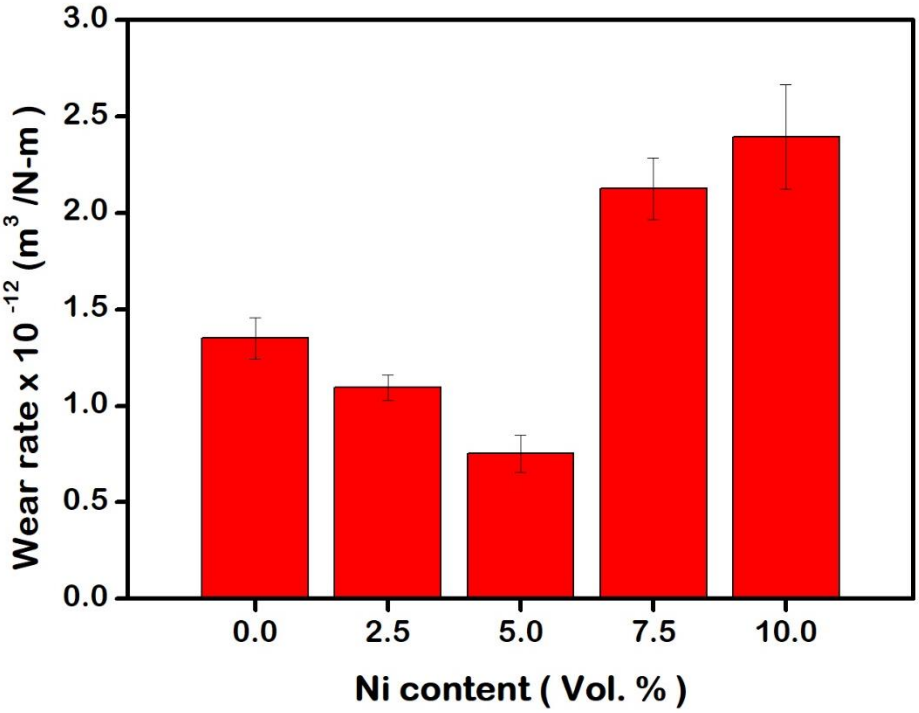

Fig. 35 Variation in wear rate of composites with the volume fraction of nickel.

Additionally, micro-cutting was observed at the edges leading to the cracking of these patches and formation of microscopic debris of 3µm in size agglomerated (cold-welded to) on the surface as observed in Fig. 36(c) & 36(d) indicating adhesive wear phenomenon. Hence, the wear mechanism was a combination of both abrasive and adhesive wear with the S5 sample exhibiting the lowest wear rate. Thus, it can be concluded that although nickel reinforcement improved the toughness, upon reinforcement beyond 5% volume fraction, the decrease in wear resistance due to a decrease in hardness of the composite dominated the wear rate more than the improved toughness of the matrix that was reflected in the increase in wear rate. Therefore, reinforcement of nickel to 5% appears to be a highly promising technique in improving the wear resistance of the composites by toughening the matrix.

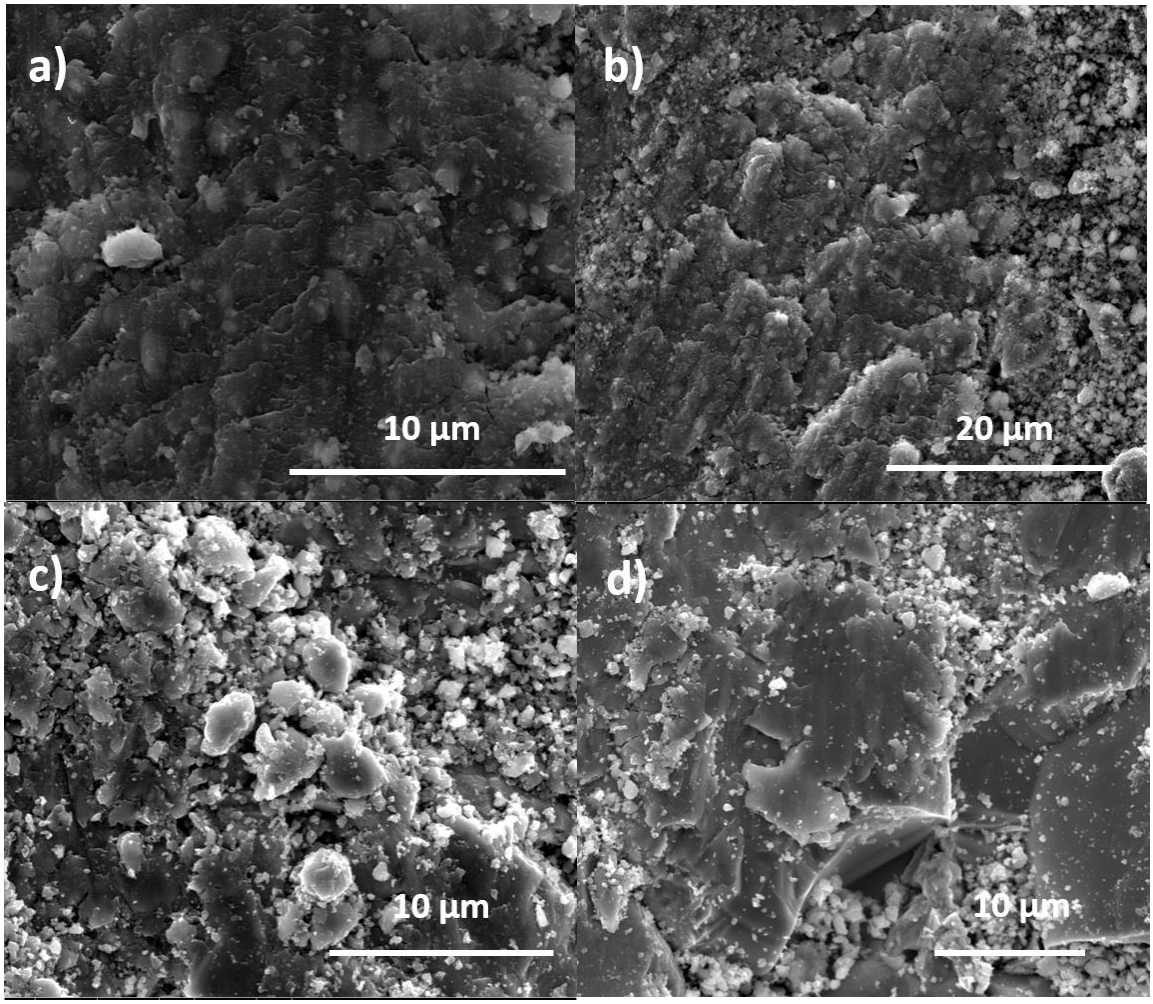

Fig. 36 SEM micrographs of worn surfaces of composites with (a) 2.5, (b) 5, (c) 7.5, and (d) 10 % nickel.

3.2.2 Electroless deposition of Nickel as a coating on Fe-based metallic glass powders

Nickel as a reinforcement was found to improve the plasticity of Zr-based metallic glasses. As an alternative to crystalline reinforcement, the effect of electroless deposition of nickel as a coating on Fe-based metallic glass powders was studied in this experiment. The Fe-based metallic glass powders were immersed and coated in a commercially available electroless nickel solution. The nickel can be found to be deposited as a layer of 6 µm around the metallic powders. The powders were systematically cleaned before and after the coating process. The coated powders were then sintered.

3.2.2.1 Microstructure

The SEM micrographs of the coated powders are displayed in Fig. 37. It can be clearly seen that the coating on the powders is not as uniform as desired. Although the average thickness of the coating was measured to be 6 µm, agglomeration of nickel was observed around certain particles. Different methods were employed to mix and stir the powders in the solution during the coating process to ensure uniform deposition of nickel on the powders. However, due to insufficient time during which the powders were suspended in the solution, the coatings were obtained only on 80 % of the surface area of the powders. The coated powders were sintered, and the microstructure of the composite was analyzed. As seen in Fig. 38 the microstructure of the composite clearly displays severe agglomeration of nickel in the matrix. Fe-based metallic glass powders can be seen inside the nickel pool. Failure to achieve uniform distribution of nickel can be responsible for the poor corrosion and wear performance of the metallic glass composites.

3.2.2.1 Phase Analysis

The phase analysis of the sintered composite is exhibited in Fig.39. It is evident that a crystalline peak is superimposed over a halo diffraction peak, that corresponds to the amorphous phase of the metallic glass matrix in the composite. The possible intermetallic phases formed in the composite are indexed to their corresponding peaks in the XRD pattern. As Fe constitutes a major fraction of

the metallic glass composition, it is believed that most of the phases formed are of the type Fe_xNi_y.

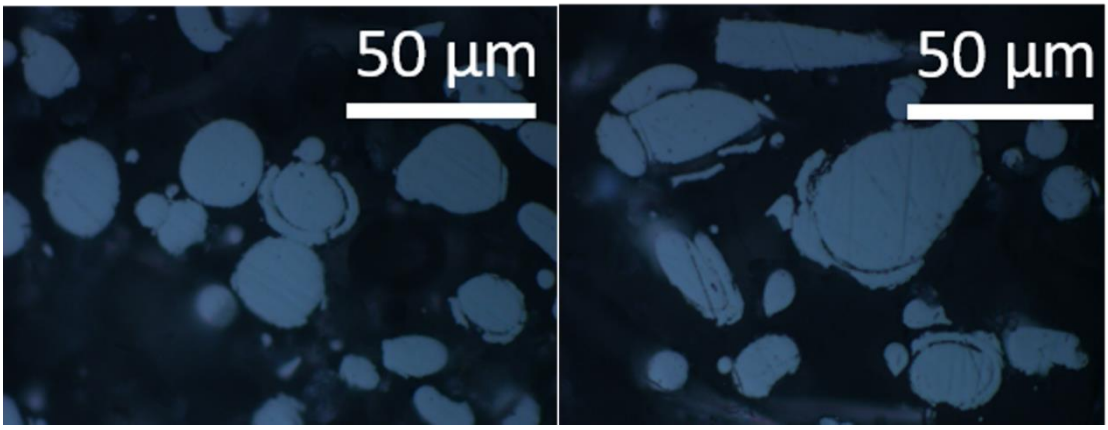

Fig. 37 SEM micrograph of electroless nickel coated Fe-based metallic glass powders**.**

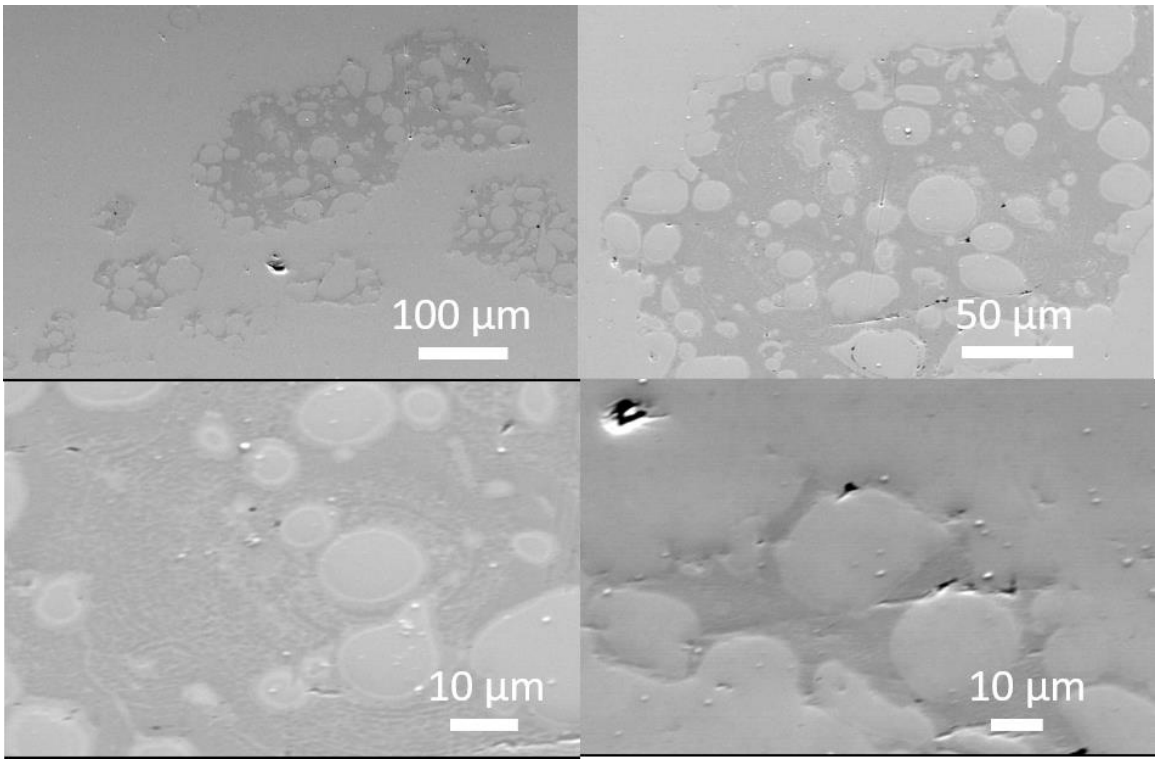

Fig. 38 SEM micrograph of sintered electroless nickel coated Fe-based metallic glass powders.

However, as the commercial electroless nickel solution used to coat the metallic glass powders contains 5 % phosphorous, it can be assumed that a fraction of phosphorous is present in the

nickel deposited on the powders. However, the presence of phosphorous in any of the intermetallic phases is debatable and open to speculation, due to the overlapping of those phases with other intermetallic compounds.

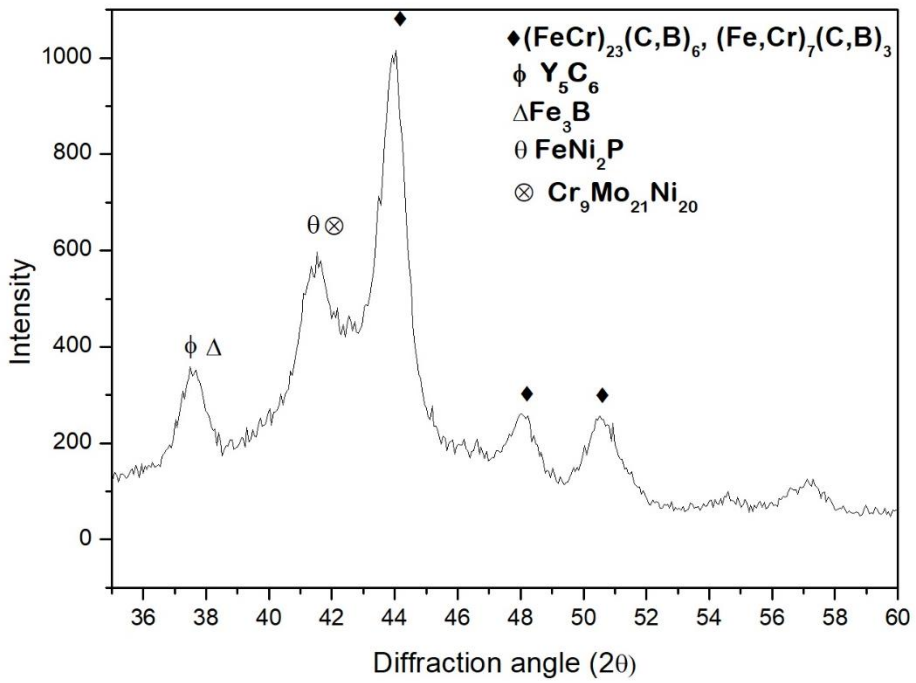

Fig. 39 XRD pattern of electroless nickel coated and sintered Fe-based metallic glass composites.

3.2.2.2 Wear and Corrosion analysis

The electrochemical behavior of the sintered composites is presented and compared with that of the monolithic alloy in Fig.40. Contrary to the behavior exhibited by the composites containing crystalline nickel, these electroless nickel reinforced composites display corrosion resistance close to that of the monolithic alloy. This superior corrosion resistance can be attributed to the presence or lack of electroless nickel. It is believed that the nickel deposited around the Fe-based metallic glass particles was inhomogeneous, resulting in the lack of uniform distribution of nickel in the composite. Therefore, it is concluded that the volume fraction of nickel present in the composite is not sufficient to influence the corrosion behavior significantly. In addition, as

electroless nickel exhibits a crystallization temperature around 400 ˚C, the nickel in the sintered composite, even in minute volume fraction, is crystalline and therefore causes deteriorated corrosion performance when compared to the monolithic alloy.

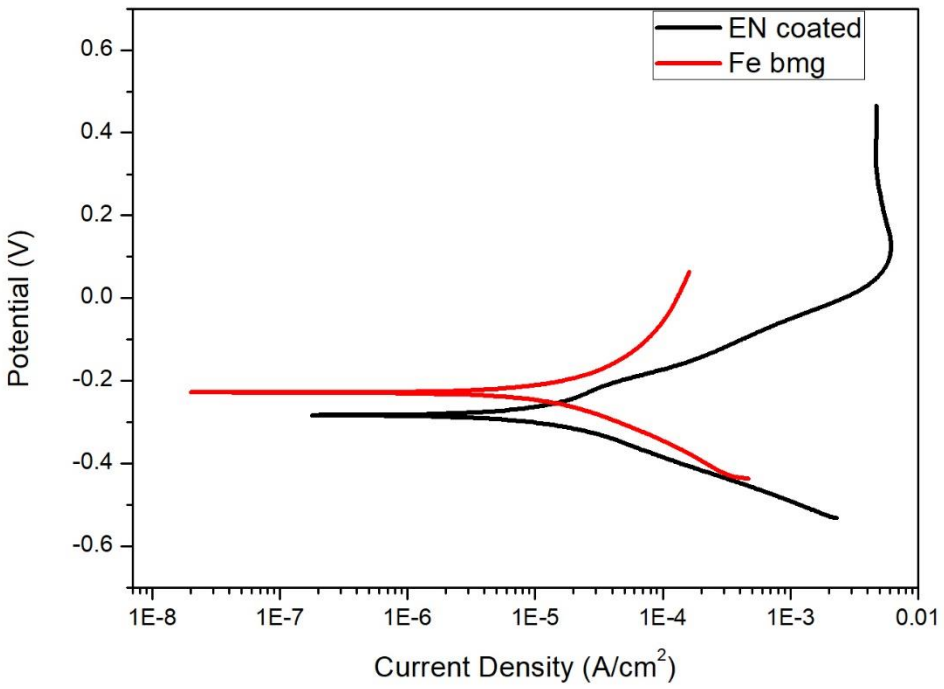

Fig. 40 Potentiodynamic polarization curve of electroless nickel reinforced Fe-based metallic glass composite.

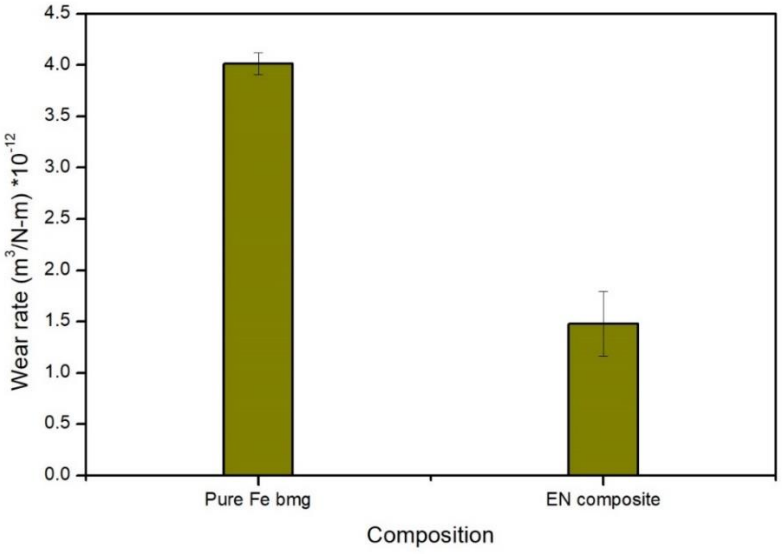

Fig. 41 Comparison of wear rate between monolithic alloy and electroless nickel reinforced metallic glass composite.

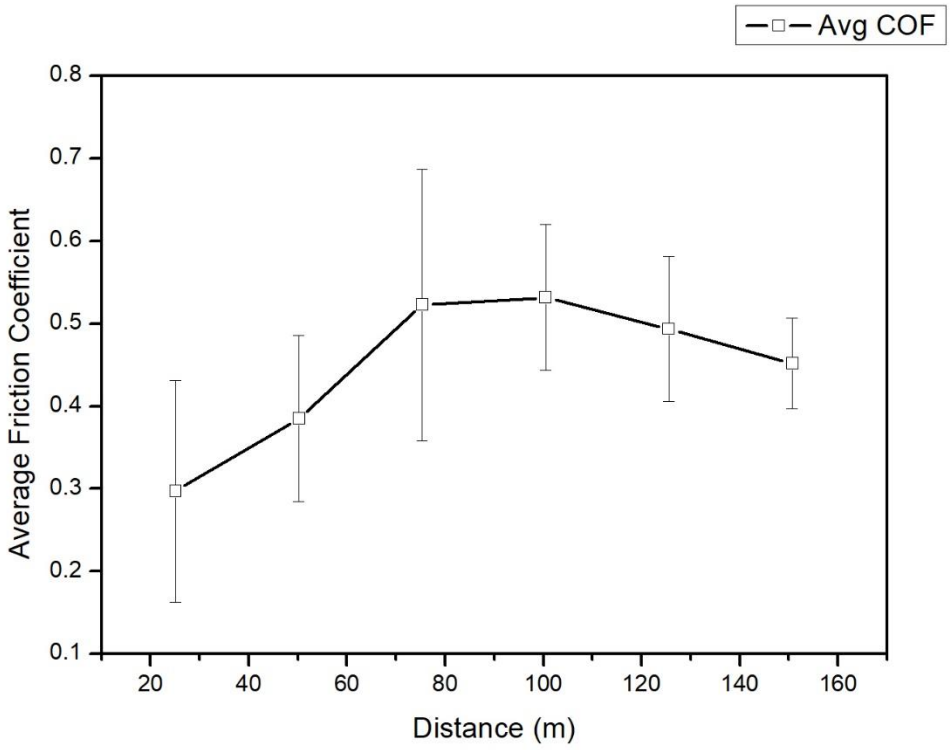

Fig. 42 Variation in friction coefficient with sliding distance**.**

The sliding wear behavior of the sintered composites is compared to that of the monolithic alloy. Although the wear rate of the composites is lower than the monolithic metallic glass, the value is comparable to the wear of pure metallic glass alloy from other experiments. The trend in variation of friction coefficient also represents the theory of running in and steady-state conditions of friction coefficient with sliding distance, observed in most metallic glasses. This not only reveals the dependence of wear tests on various testing conditions but also questions the presence of the nickel in the composite.

CHAPTER IV

CONCLUSIONS

4.1 Conclusions from Spark plasma sintering of $Fe_{48}Cr_{15}Mo_{14}Y_2C_{15}B_6$ metallic glass powder on Cu–10%Ni alloy.

Processing of Fe-based amorphous coatings of composition $Fe_{48}Cr_{15}Mo_{14}Y_2C_{15}B_6$ on Cu–10%Ni alloy substrates is reported using spark plasma sintering. The sintered coatings exhibited high density with hardness (1200-1400 HV) close to the sintered monolithic bulk amorphous alloy of similar compositions. While the sintering temperatures (575-675 ˚C) recorded using a thermocouple placed in the die were in the supercooled liquid region of the alloy, partial devitrification of the coatings was observed. The degree of devitrification in the amorphous coatings as observed in the x-ray analysis increased with increasing sintering temperature. The volume wear rate of the coatings showed a general decreasing trend with increasing sintering temperature in the range of 575-650 ˚C due to surface hardening and formation of a protective surface layer associated with partial devitrification. The coatings sintered at a higher temperature (675 ˚C) exhibited significantly higher wear rate due to embrittlement associated with excessive devitrification and delamination of the protective surface layer.

4.2 Conclusions from spark plasma sintering of Ni-reinforced Fe-based metallic glass composites.

In this study, the effects of increasing Ni reinforcement content (2.5 to 10 vol.%) on microstructure and corrosion and wear behavior of SPS sintered Fe-based bulk metallic glass composites are investigated. The composites exhibited dense microstructure while retaining predominantly amorphous structure of the matrix. While all the composites exhibited lower corrosion, resistance compared to monolithic metallic glass, the composites with lower reinforcement content (2.5 and 5 vol.% Ni) showed some degree of passivation in HCL solution. As Ni is a relatively softer phase, the microhardness of the glassy composites also decreased continuously with increasing Ni reinforcement content. In spite of their lower hardness, the composites with lower reinforcement content (2.5 and 5 vol.% Ni) exhibited improved sliding wear resistance due to higher toughness of the composites. The transition in wear mechanism from predominantly abrasive to adhesive at higher Ni content resulted in severe wear of the composites. The results show that Fe-based metallic glass composites with lower reinforcement content (2.5 to 5 vol.% Ni) are promising in applications where optimum corrosion and wear performance is desired.

In conclusion, spark plasma sintering can be used as an effective manufacturing method to sinter dense Fe-based amorphous alloy composites and coatings that exhibit high hardness, superior wear resistance, and controlled corrosion resistance.

.

REFERENCES

[1] amorphous metal. https://www.reade.com/products/amorphous-metals.
[2] K. Yang, D. Hitchcock, J. He, A.M. Rao, Tuning Electrical Properties of Carbon Nanotubes via Spark Plasma Sintering, in: B. Bhushan (Ed.), Encyclopedia of Nanotechnology, Springer Netherlands, Dordrecht, 2012, pp. 2780-2788.
[3] J. Karger-Kocsis, A. Mousa, Z. Major, N. Békési, Dry friction and sliding wear of EPDM rubbers against steel as a function of carbon black content, 2008.
[4] T. Bellezze, G. Giuliani, G. Roventi, Study of stainless steels corrosion in a strong acid mixture. Part 1: cyclic potentiodynamic polarization curves examined by means of an analytical method, Corrosion Science 130 (2018) 113-125.
[5] W.L. Johnson, Bulk amorphous metal—An emerging engineering material, JOM 54(3) (2002) 40-43.
[6] G. He, Z.F. Zhang, W. Löser, J. Eckert, L. Schultz, Effect of Ta on glass formation, thermal stability and mechanical properties of a Zr52.25Cu28.5Ni4.75Al9.5Ta5 bulk metallic glass, Acta Materialia 51(8) (2003) 2383-2395.
[7] Y.F. Sun, B.C. Wei, Y.R. Wang, W.H. Li, T.L. Cheung, C.H. Shek, Plasticity-improved Zr–Cu–Al bulk metallic glass matrix composites containing martensite phase, Applied Physics Letters 87(5) (2005) 051905.
[8] J.-J. Oak, D.V. Louzguine-Luzgin, A. Inoue, Investigation of glass-forming ability, deformation and corrosion behavior of Ni-free Ti-based BMG alloys designed for application as dental implants, Materials Science and Engineering: C 29(1) (2009) 322-327.
[9] C.L. Qin, J.J. Oak, N. Ohtsu, K. Asami, A. Inoue, XPS study on the surface films of a newly designed Ni-free Ti-based bulk metallic glass, Acta Materialia 55(6) (2007) 2057-2063.
[10] S. Yi, T.G. Park, D.H. Kim, Ni-based bulk amorphous alloys in the Ni–Ti–Zr–(Si, Sn) system, Journal of Materials Research 15(11) (2011) 2425-2430.
[11] B. Prakash, Abrasive wear behaviour of Fe, Co and Ni based metallic glasses, Wear 258(1) (2005) 217-224.
[12] A. Kawashima, H. Habazaki, K. Hashimoto, Highly corrosion-resistant Ni-based bulk amorphous alloys, Materials Science and Engineering: A 304-306 (2001) 753-757.
[13] J. Sort, D.C. Ile, A.P. Zhilyaev, A. Concustell, T. Czeppe, M. Stoica, S. Suriñach, J. Eckert, M.D. Baró, Cold-consolidation of ball-milled Fe-based amorphous ribbons by high pressure torsion, Scripta Materialia 50(9) (2004) 1221-1225.
[14] S.L. Wang, H.X. Li, X.F. Zhang, S. Yi, Effects of Cr contents in Fe-based bulk metallic glasses on the glass forming ability and the corrosion resistance, Materials Chemistry and Physics 113(2-3) (2009) 878-883.
[15] S. Yoon, J. Kim, B.D. Kim, C. Lee, Tribological behavior of B4C reinforced Fe-base bulk metallic glass composite coating, Surface and Coatings Technology 205(7) (2010) 1962-1968.
[16] A. Reardon, Discovering metals–a historical overview, Metallurgy for the non-metallurgist (2011) 73-84.

[17] K.G. Budinski, M.K. Budinski, Engineering Materials: Properties and Selection, Prentice Hall2010.
[18] P. Fischer, V. Romano, A. Blatter, H.P. Weber, Highly precise pulsed selective laser sintering of metallic powders, Laser Physics Letters 2(1) (2005) 48.
[19] T. Itoi, T. Takamizawa, Y. Kawamura, A. Inoue, Fabrication of Co40Fe22Nb8B30 bulk metallic glasses by consolidation of gas-atomized powders and their soft-magnetic properties, Scripta Materialia 45(10) (2001) 1131-1137.
[20] W.H. Wang, C. Dong, C.H. Shek, Bulk metallic glasses, Materials Science and Engineering: R: Reports 44(2–3) (2004) 45-89.
[21] A.L. Greer, K.L. Rutherford, I.M. Hutchings, Wear resistance of amorphous alloys and related materials, International Materials Reviews 47(2) (2002) 87-112.
[22] W. Chen, U. Anselmi-Tamburini, J.E. Garay, J.R. Groza, Z.A. Munir, Fundamental investigations on the spark plasma sintering/synthesis process: I. Effect of dc pulsing on reactivity, Materials Science and Engineering: A 394(1) (2005) 132-138.
[23] T. Paul, S.P. Harimkar, Initial stage densification during spark plasma sintering of Fe-based amorphous alloy powder: Analysis of viscous flow, Journal of Applied Physics 120(13) (2016) 134901.
[24] P. Tanaji, P.H. Sandip, Prediction of heating rate controlled viscous flow activation energy during spark plasma sintering of amorphous alloy powders, Journal of Physics D: Applied Physics 50(27) (2017) 27LT01.
[25] T. Paul, S.P. Harimkar, Viscous flow activation energy adaptation by isochronal spark plasma sintering, Scripta Materialia 126 (2017) 37-40.
[26] X.-Y. Fu, D.A. Rigney, Tribological Characteristics of Zr41.2Ti13.8Cu12.5Ni10.0Be22.5 Bulk Metallic Glass, MRS Proceedings 554 (2011).
[27] T. Paul, N. Chawake, R.S. Kottada, S.P. Harimkar, Pressure controlled micro-viscous deformation assisted spark plasma sintering of Fe-based bulk amorphous alloy, Journal of Alloys and Compounds 738 (2018) 10-15.
[28] T. Paul, A. Loganathan, A. Agarwal, S.P. Harimkar, Kinetics of isochronal crystallization in a Fe-based amorphous alloy, Journal of Alloys and Compounds 753 (2018) 679-687.
[29] I. Hutchings, P. Shipway, Tribology: Friction and Wear of Engineering Materials, Elsevier Science2017.
[30] I. Hutchings, P. Shipway, Tribology: Friction and wear of engineering materials: Second Edition, 2017.
[31] B.D. Craig, A. International, Handbook of corrosion data, ASM International1989.
[32] D.C. Silverman, Tutorial on Cyclic Potentiodynamic Polarization Technique, CORROSION 98, NACE International, San Diego, California, 1998.
[33] M. Stern, A.L. Geary, Electrochemical Polarization: I . A Theoretical Analysis of the Shape of Polarization Curves, Journal of The Electrochemical Society 104(1) (1957) 56-63.
[34] R.S. Jiang, Y.T. Wang, L. Hu, G. Xu, Z.D. Liu, Effect of Mo Content on the Corrosion Resistance of Fe-Based Amorphous Composite Coating, Materials Science Forum 849 (2016) 636-641.
[35] Z. Kovács, E. Schafler, P. Szommer, Á. Révész, Localization of plastic deformation along shear bands in Vitreloy bulk metallic glass during high pressure torsion, Journal of Alloys and Compounds 593 (2014) 207-212.

[36] Z. Bian, M.X. Pan, Y. Zhang, W.H. Wang, Carbon-nanotube-reinforced Zr52.5Cu17.9Ni14.6Al10Ti5 bulk metallic glass composites, Applied Physics Letters 81(25) (2002) 4739-4741.
[37] Y.H. Lai, C.J. Lee, Y.T. Cheng, H.S. Chou, H.M. Chen, X.H. Du, C.I. Chang, J.C. Huang, S.R. Jian, J.S.C. Jang, T.G. Nieh, Bulk and microscale compressive behavior of a Zr-based metallic glass, Scripta Materialia 58(10) (2008) 890-893.
[38] J.M. Park, Y.C. Kim, W.T. Kim, D.H. Kim, Ti-Based Bulk Metallic Glasses with High Specific Strength, MATERIALS TRANSACTIONS 45(2) (2004) 595-598.
[39] Y. Huang, J. Shen, J. Sun, Z. Zhang, Enhanced strength and plasticity of a Ti-based metallic glass at cryogenic temperatures, Materials Science and Engineering: A 498(1-2) (2008) 203-207.
[40] M.L. Morrison, R.A. Buchanan, A. Peker, P.K. Liaw, J.A. Horton, Electrochemical behavior of a Ti-based bulk metallic glass, Journal of Non-Crystalline Solids 353(22-23) (2007) 2115-2124.
[41] Y.C. Kim, J.H. Na, J.M. Park, D.H. Kim, J.K. Lee, W.T. Kim, Role of nanometer-scale quasicrystals in improving the mechanical behavior of Ti-based bulk metallic glasses, Applied Physics Letters 83(15) (2003) 3093-3095.
[42] G. He, W. Löser, J. Eckert, L. Schultz, Enhanced plasticity in a Ti-based bulk metallic glass-forming alloy by in situ formation of a composite microstructure, Journal of Materials Research 17(12) (2011) 3015-3018.
[43] T. Zhang, A. Inoue, New Bulk Glassy Ni-Based Alloys with High Strength of 3000 MPa, MATERIALS TRANSACTIONS 43(4) (2002) 708-711.
[44] D. Liu, W. Gao, Z. Li, H. Zhang, Z. Hu, Electro-spark deposition of Fe-based amorphous alloy coatings, Materials Letters 61(1) (2007) 165-167.
[45] D.Z. Segu, J.-H. Choi, S.-S. Kim, Sliding wear behavior of Fe-based bulk metallic glass at high temperature, Journal of Mechanical Science and Technology 26(11) (2012) 3565-3570.
[46] M.S. Parvizi, A. Aladjem, J.E. Castle, Behaviour of 90–10 cupronickel in sea water, International Materials Reviews 33(1) (1988) 169-200.
[47] J.M. Popplewell, R.J. Hart, J.A. Ford, The effect of iron on the corrosion characteristics of 90-10 cupro nickel in quiescent 3·4%NaCl solution, Corrosion Science 13(4) (1973) 295-309.
[48] W. Schleich, K. Steinkamp, Biofouling Resistance of Cupronickel -Basics and Experience, Stainless Steel World Conference, Maastricht, 2003.
[49] Y.H. Yoo, S.H. Lee, J.G. Kim, J.S. Kim, C. Lee, Effect of heat treatment on the corrosion resistance of Ni-based and Cu-based amorphous alloy coatings, Journal of Alloys and Compounds 461(1–2) (2008) 304-311.
[50] J.B. Cheng, X.B. Liang, B.S. Xu, Y.X. Wu, Characterization of mechanical properties of FeCrBSiMnNbY metallic glass coatings, Journal of Materials Science 44(13) (2009) 3356-3363.
[51] T. Zhang, F. Liu, S. Pang, R. Li, Ductile Fe-Based Bulk Metallic Glass with Good Soft-Magnetic Properties, Materials transactions 48(5) (2007) 1157-1160.
[52] B.L. Shen, H. Kimura, A. Inoue, Fabrication of Fe-based glassy cores with high saturation magnetization and good soft magnetic properties by spark plasma sintering, in: Z.Y. Zhong, H. Saka, T.H. Kim, E.A. Holm, Y.F. Han, X.S. Xie (Eds.), Pricm 5: The

Fifth Pacific Rim International Conference on Advanced Materials and Processing, Pts 1-52005, pp. 3397-3400.
[53] J.J. Lewandowski, X.J. Gu, A.S. Nouri, S.J. Poon, G.J. Shiflet, Tough Fe-based bulk metallic glasses, Applied Physics Letters 92(9) (2008) 091918.
[54] A. Inoue, B.L. Shen, C.T. Chang, Super-high strength of over 4000 MPa for Fe-based bulk glassy alloys in [(Fe1−xCox)0.75B0.2Si0.05]96Nb4 system, Acta Materialia 52(14) (2004) 4093-4099.
[55] K.F. Yao, C.Q. Zhang, Fe-based bulk metallic glass with high plasticity, Applied Physics Letters 90(6) (2007) 061901.
[56] C. Zhang, L. Liu, K.C. Chan, Q. Chen, C.Y. Tang, Wear behavior of HVOF-sprayed Fe-based amorphous coatings, Intermetallics 29 (2012) 80-85.
[57] W. Yuping, L. Pinghua, C. Chenglin, W. Zehua, C. Ming, H. Junhua, Cavitation erosion characteristics of a Fe–Cr–Si–B–Mn coating fabricated by high velocity oxy-fuel (HVOF) thermal spray, Materials Letters 61(8–9) (2007) 1867-1872.
[58] H.S. Ni, X.H. Liu, X.C. Chang, W.L. Hou, W. Liu, J.Q. Wang, High performance amorphous steel coating prepared by HVOF thermal spraying, Journal of Alloys and Compounds 467(1–2) (2009) 163-167.
[59] K. Hildal, N. Sekido, J.H. Perepezko, Critical cooling rate for Fe48Cr15Mo14Y2C15B6 bulk metallic glass formation, Intermetallics 14(8–9) (2006) 898-902.
[60] J. Kim, K. Kang, S. Yoon, S. Kumar, H. Na, C. Lee, Oxidation and crystallization mechanisms in plasma-sprayed Cu-based bulk metallic glass coatings, Acta Materialia 58(3) (2010) 952-962.
[61] F. Otsubo, K. Kishitake, Corrosion Resistance of Fe-16%Cr-30%Mo-(C,B,P) Amorphous Coatings Sprayed by HVOF and APS Processes, Materials Transactions 46(1) (2005) 80-83.
[62] K. Chokethawai, D.G. McCartney, P.H. Shipway, Microstructure evolution and thermal stability of an Fe-based amorphous alloy powder and thermally sprayed coatings, Journal of Alloys and Compounds 480(2) (2009) 351-359.
[63] S. Yoon, J. Kim, G. Bae, B. Kim, C. Lee, Formation of coating and tribological behavior of kinetic sprayed Fe-based bulk metallic glass, Journal of Alloys and Compounds 509(2) (2011) 347-353.
[64] Z. Zhou, L. Wang, F.-c. Wang, Y.-b. Liu, Formation and corrosion behavior of Fe-based amorphous metallic coatings prepared by detonation gun spraying, Transactions of Nonferrous Metals Society of China 19 (2009) s634-s638.
[65] T. Paul, S.H. Alavi, S. Biswas, S.P. Harimkar, Microstructure and Wear Behavior of Laser Clad Multi-layered Fe-based Amorphous Coatings on Steel Substrates, Lasers in Manufacturing and Materials Processing 2(4) (2015) 231-241.
[66] A.H. Pakseresht, A.H. Javadi, M. Bahrami, F. Khodabakhshi, A. Simchi, Spark plasma sintering of a multilayer thermal barrier coating on Inconel 738 superalloy: Microstructural development and hot corrosion behavior, Ceramics International 42(2, Part A) (2016) 2770-2779.
[67] F. Nozahic, C. Estournès, A.L. Carabat, W.G. Sloof, S. van der Zwaag, D. Monceau, Self-healing thermal barrier coating systems fabricated by spark plasma sintering, Materials & Design.

[68] A. Singh, S.R. Bakshi, A. Agarwal, S.P. Harimkar, Microstructure and tribological behavior of spark plasma sintered iron-based amorphous coatings, Materials Science and Engineering: A 527(18) (2010) 5000-5007.
[69] M. Tokita, Mechanism of spark plasma sintering, Proceeding of NEDO International Symposium on Functionally Graded Materials, Japan, 1999, pp. 1-13.
[70] U. Anselmi-Tamburini, S. Gennari, J.E. Garay, Z.A. Munir, Fundamental investigations on the spark plasma sintering/synthesis process: II. Modeling of current and temperature distributions, Materials Science and Engineering: A 394(1) (2005) 139-148.
[71] T.Q. Phan, J.P. Kelly, M.E. Kassner, V. Eliasson, O.A. Graeve, A.M. Hodge, Bulk Mechanical Properties Testing of Metallic Marginal Glass Formers, Journal of Metallurgy 2016 (2016) 8.
[72] J.P. Kelly, S.M. Fuller, K. Seo, E. Novitskaya, V. Eliasson, A.M. Hodge, O.A. Graeve, Designing in situ and ex situ bulk metallic glass composites via spark plasma sintering in the super cooled liquid state, Materials & Design 93 (2016) 26-38.
[73] S.P. Harimkar, S.R. Paital, A. Singh, R. Aalund, N.B. Dahotre, Microstructure and properties of spark plasma sintered Fe-Cr-Mo-Y-B-C bulk metallic glass, Journal of Non-Crystalline Solids 355(43-44) (2009) 2179-2182.
[74] A. Singh, S.P. Harimkar, Spark plasma sintering of in situ and ex situ iron-based amorphous matrix composites, Journal of Alloys and Compounds 497(1–2) (2010) 121-126.
[75] M. Telford, The case for bulk metallic glass, Materials today 7(3) (2004) 36-43.
[76] H.M. Ha, J.H. Payer, Devitrification of Fe-based amorphous metal SAM 1651: a structural and compositional study, Metallurgical and Materials Transactions A 40(11) (2009) 2519-2529.
[77] C.K. Kim, S. Lee, S.Y. Shin, D.H. Kim, Microstructure and mechanical properties of Cu-base amorphous alloy matrix composites consolidated by spark plasma sintering, Materials Science and Engineering: A 449–451 (2007) 924-928.
[78] D. Kwon, E. Park, M. Huh, H. Kim, J. Bae, Wear behavior of Fe-based bulk metallic glass composites, Journal of Alloys and Compounds 509 (2011) S105-S108.
[79] A. Singh, S. Katakam, J. Ilavsky, N.B. Dahotre, S.P. Harimkar, Nanocrystallization in spark plasma sintered Fe48Cr15Mo14Y2C15B6 bulk amorphous alloy, Journal of Applied Physics 114(5) (2013) 054903.
[80] T. Paul, A. Singh, S.P. Harimkar, Densification and Crystallization in Fe–Based Bulk Amorphous Alloy Spark Plasma Sintered in the Supercooled Liquid Region , Advanced Engineering Materials, Advanced Engineering Materials, 2017.
[81] S.P. Harimkar, S.R. Paital, A. Singh, R. Aalund, N.B. Dahotre, Microstructure and properties of spark plasma sintered Fe–Cr–Mo–Y–B–C bulk metallic glass, Journal of Non-Crystalline Solids 355(43) (2009) 2179-2182.
[82] K. Kishitake, H. Era, F. Otsubo, Characterization of plasma sprayed Fe-17Cr-38Mo-4C amorphous coatings crystallizing at extremely high temperature, Journal of Thermal Spray Technology 5(3) (1996) 283-288.
[83] J. Cheng, X. Liang, B. Xu, Y. Wu, Formation and properties of Fe-based amorphous/nanocrystalline alloy coating prepared by wire arc spraying process, Journal of Non-Crystalline Solids 355(34–36) (2009) 1673-1678.

[84] A. Singh, S.R. Paital, A. Andapally, N.B. Dahotre, S.P. Harimkar, Densification Behavior and Wear Response of Spark Plasma Sintered Iron-Based Bulk Amorphous Alloys, Advanced Engineering Materials 14(6) (2012) 400-407.
[85] S.P. Harimkar, S.R. Paital, A. Singh, R. Aalund, N.B. Dahotre, Microstructure and properties of spark plasma sintered Fe–Cr–Mo–Y–B–C bulk metallic glass, Journal of Non-Crystalline Solids 355(43-44) (2009) 2179-2182.
[86] Q. Chen, S. Guo, X. Yang, X. Zhou, X. Hua, X. Zhu, Z. Duan, Study on corrosion resistance of Fe-based amorphous coating by laser cladding in hydrochloric acid, Physics Procedia 50 (2013) 297-303.
[87] P.A. Hess, S.J. Poon, G. Shiflet, R.H. Dauskardt, Indentation fracture toughness of amorphous steel, Journal of materials research 20(4) (2005) 783-786.

VITA

Himabindu Kasturi
Candidate for the Degree of

Master of Science

Thesis: WEAR AND CORROSION BEHAVIOR OF SPARK PLASMA SINTERED IRON-BASED BULK METALLIC GLASS COMPOSITES AND COATINGS

Major Field: Mechanical and Aerospace Engineering

Biographical:

Education:

Completed the requirements for the Master of Science in Mechanical and Aerospace Engineering at Oklahoma State University, Stillwater, Oklahoma in July, 2018.

Completed the requirements for the Bachelor of Science in Mechanical Engineering at MVSR Engineering College, Osmania University, Hyderabad, Telangana, India in 2014.

Experience: GTP, ARCI India, 2014-2015.

Professional Memberships: SAE